Ludwig-Maximilians-University Munich

Reproducible Superconducting Contacts to Graphene-Based Heterostructures

Master Thesis

Daniil Ivanov

Chair of Experimental Solid State Physics
Quantum Materials

Supervisors:
Andrés Díez Carlón
Prof. Dr. Dmitri K. Efetov

23.10.2024

Ludwig-Maximilians-Universität München

Reproduzierbare supraleitende Kontakte zu Graphen-basierten Heterostrukturen

Masterarbeit

vorgelegt von
Daniil Ivanov

Quantenmaterialien Gruppe
Fakultät für Physik

Betreuer: **Prof. Dr. Dmitri K. Efetov**
Weiterer Betreuer: **Andrés Díez Carlón**

23.10.2024

Contents

1 Introduction

After Andre Geim and Konstantin Novoselov discovered graphene in 2004 [1], the two-dimensional physics experienced exponential growth. An abundance of various monolayer materials, with physical properties significantly different from those of their bulk origin, was predicted and synthesized. Soon after, people realized that if vertically assembled, the resulting structure might obtain unexpected properties distinct from the separate layers. As a result, the vertical assembly created a unique platform for the discovery of a limitless range of 2D material combinations. The field evolved once more when people realized that the materials could be assembled with rotation angles relative to each other. This additional degree of freedom in the fabrication process resulted in the discovery of systems supporting several unique phenomena: correlated insulators, magnetism, unconventional superconductivity, anomalous quantum Hall effect, and strange metal states. The nature of many of these phenomena is yet to be fully understood.

One promising experimental platform that could shed light on the nature of these phases are Josephson junctions, where the induced superconductivity is affected by the intrinsic state of the 2D material. In the special case of bilayer graphene rotated by 1.1° relative to each other, for example, the properties of the intrinsic superconductivity could be explored by creating Josephson junctions with different orientations.

To implement such an experimental system, a good-quality contact between superconducting leads and the 2D material is needed. The main goal of this master's thesis was to develop a reliable fabrication recipe for superconducting MoRe contacts in graphene-based heterostructures. After accomplishing this goal, this recipe was used to fabricate and characterize Josephson junctions based on monolayer graphene encapsulated with hBN.

The thesis is structured as follows: the first chapter provides a theoretical overview of superconductivity and graphene physics. The second chapter describes the fabrication techniques used to manufacture the graphene-based devices, including the developed sputtering recipe for MoRe deposition. The third chapter presents the analysis of Josephson junction devices made from both aligned and non-aligned graphene-hBN heterostructures.

2 Theoretical Background

2.1 Superconductivity and Josephson Junction

2.1.1 Superconductivity

Superconductivity is a phenomenon first observed in 1911 by H. Kamerlingh Onnes[2], which refers to the complete disappearance of electrical resistance in certain materials below a critical temperature, T_c. Later, it was found by Meissner and Ochsenfeld that these materials also behave like perfect diamagnets[3], almost completely excluding magnetic flux from the interior of a superconductor. The magnetic field penetrates the superconductor only on the scale of the penetration length λ_L. [4]. These two discoveries imply that the superconductor will retain its properties as long as it is not warmed above the critical temperature T_c, the current does not exceed its critical value I_c, or it is not exposed to a magnetic field higher than the critical field.

The most successful theory describing this phenomenon is the Bardeen-Cooper-Schrieffer (BCS) theory[5]. According to this theory, in the presence of the Fermi sea, even a small attractive force between electrons (such as one caused by electron-phonon interaction) causes two electrons with opposite spin and momentum to form a bound state called a Cooper pair, which has a spatial length on the order of ξ_0. Notably, because paired electrons obey bosonic statistics, they form a condensate defined by a global wavefunction $\psi \sim |\psi|e^{i\phi}$ shared by all pairs of electrons, preserving phase coherence over significant distances.

The bound energy of a Cooper pair, Δ, leads to the formation of an energy gap $E_g = 2\Delta$, which is the minimum amount of energy required to break a Cooper pair. The theory predicts the value of the energy gap and coherence length as:

$$\Delta \approx 1.764 k_B T_c \tag{1}$$

$$\xi_0 = \frac{\hbar v_F}{\pi \Delta} \tag{2}$$

where v_F is the Fermi velocity, T_c is the critical temperature, $\hbar$ is the Plank constant, and k_B is the Boltzmann constant.

Seven years before the BCS theory, another functional theory focusing purely on the phenomenological aspect of superconductivity was developed. The Ginzburg-Landau theory [6] expresses free energy in terms of a complex wavefunction, which acts as an order parameter within a second-order phase transition. The theory also introduces the Ginzburg-Landau coherence length ξ as a measure of characteristic length.

$$\xi = \frac{\hbar}{|2m^* \alpha(T)|^{1/2}} \tag{3}$$

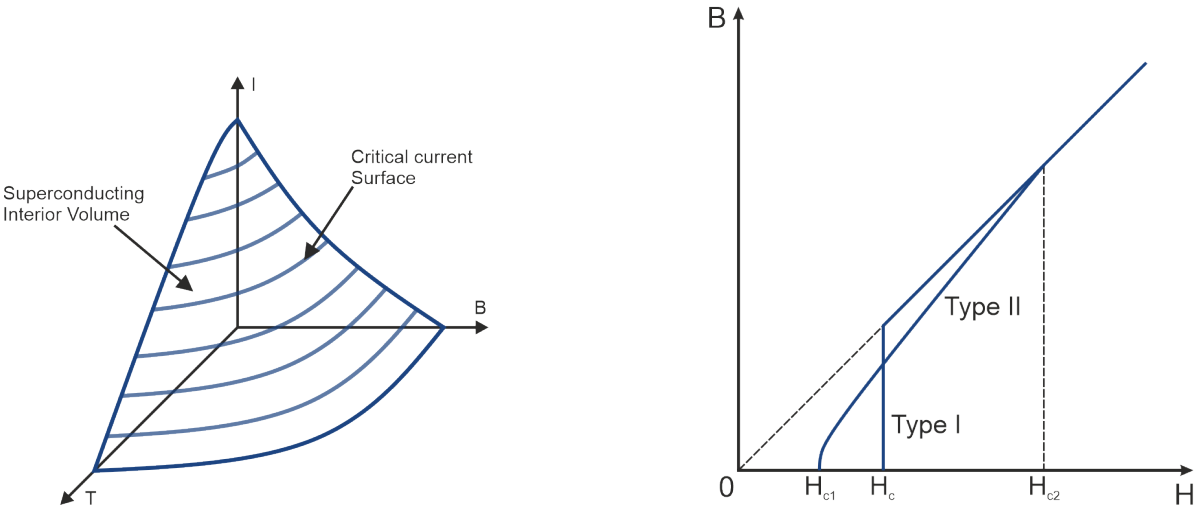

Figure 1: a: Superconductivity phase diagram as a function of current, magnetic field, and temperature. b: Magnetic field penetration behavior of type I and type II superconductors.

.

The two characteristic lengths presented by the theories, ξ_0 and ξ, though different yet related, are approximately equal to each other at temperatures significantly below T_c. They play important roles in describing key features of superconductivity.

Firstly, as proposed by Abrikosov in 1957[7], the behavior of a superconductor strongly changes with the change of a GL parameter $\kappa = \lambda_L/\xi$. For materials with $0 < \kappa < 1/\sqrt{2}$ (type I superconductors), a discontinuous collapse of superconductivity at some critical field H_c is expected. For materials with $\kappa > 1/\sqrt{2}$ (type II superconductors), a continuous phase transition occurs. At some lower critical field H_{c1}, a continuous increase in flux penetration begins, reaching its maximum value B at the upper critical field H_{c2}. Between H_{c1} and H_{c2}, the magnetic field penetrates the superconductor with supercurrent vortices carrying a magnetic flux quantum:

$$\Phi_0 = \frac{hc}{2e} \approx 2.07 \times 10^{-15}\text{Wb} \tag{4}$$

which makes type II superconductors not perfect diamagnets.

Secondly, ξ is crucial in describing the behavior of Cooper pairs at a superconductor/non-superconductor interface. In this case, superconductivity infiltrates the non-superconductor with its wave function amplitude exponentially decaying as the distance from the interface increases. This phenomenon is known as the proximity effect and is used for the formation of Josephson junctions, discussed in the upcoming section.

The BCS theory successfully describes the behavior of many superconductors. However, it fails to fully explain the superconducting properties of certain materials, thus called unconventional superconductors. Among these, there are several types of superconductors of high interest due to their high critical temperature(such as cuprates, iron-based super-

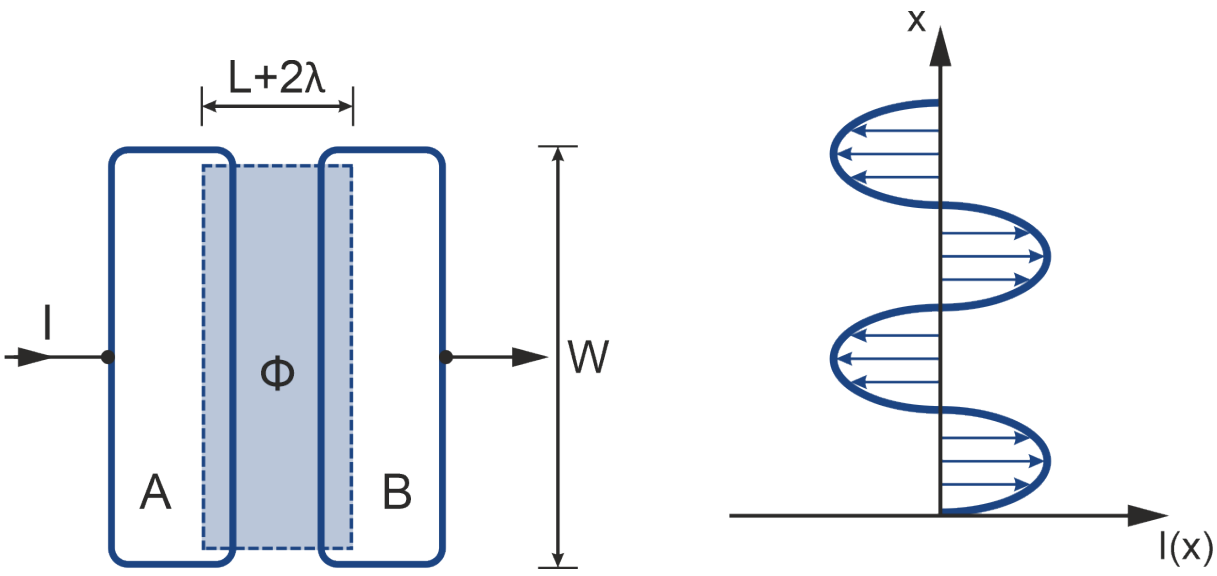

Figure 2: (a): Scheme of a junction geometry. A dashed line marks a contour for integration discussed in the main text. (b): Current distribution in a Josephson junction at a magnetic field $\Phi = 2\Phi_0$.Figures are adapted from [4]

conductors, etc.)[8–12]. Despite research providing some insight into the nature of these superconductors, such as anisotropic wavefunctions[13–18], a comprehensive theoretical model is yet to be achieved.

2.1.2 Josephson Junction

A Josephson junction(JJ) [19] is a device composed of two superconductors separated by a non-superconducting material called a weak link. Due to the proximity effect, the supercurrent can pass through the weak link even at zero voltage while the two superconductors preserve their global wavefunctions $\psi_1 \sim |\psi_1|e^{i\phi_1}$and $\psi_2 \sim |\psi_2|e^{i\phi_2}$. The Josephson effect is described by two Josephson equations. The first equation:

$$I(\phi) = I_c \sin\phi \tag{5}$$

where ϕ is the difference in the phase of the wavefunctions of the two electrodes, and I_c is the maximum supercurrent that the junction can conduct, describes the DC Josephson effect.

The second equation:

$$\frac{\mathrm{d}\phi}{\mathrm{d}t} = \frac{2e}{\hbar}V. \tag{6}$$

is called the AC Josephson effect. It implies that if there is a voltage difference V across the junction, the phase difference changes accordingly, and the current alternates with frequency $f = \frac{2eV}{h}$.

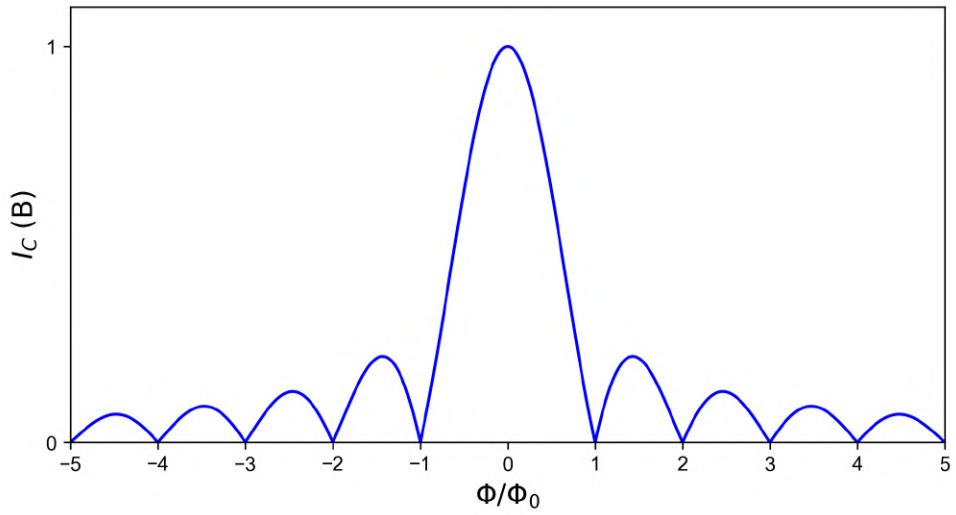

Figure 3: Fraunhofer pattern for rectangular Josephson Junction. The value of critical current is normalized.

One of the key features of the Josephson junction arises when the device is exposed to an external magnetic field. When the junction is placed under a magnetic field perpendicular to the direction of the current flow, its value changes oscillatory.

Let us consider a rectangular junction in a coordinate system such that the electrode surface is parallel to the xy plane and the current flows along the y direction. As the global wavefunction of the superconductors has to remain single-valued, by taking the line integral of the magnetic vector potential $\mathbf{A}$ ($\mathbf{B} = \nabla \times \mathbf{A}$) over the contour passing through both superconductors and the weak link, one can show that the phase accumulation is given by:

$$\Delta\phi = 2\pi \frac{\Phi}{\Phi_0} \tag{7}$$

As the flux in the closed path is given by:

$$d\Phi = Btdx \tag{8}$$

where $t = d + 2\lambda_L$, the local value of supercurrent at the Josephson junction, which is given by $I_s = I_c \sin(\Delta\phi)$, then oscillates sinusoidally with position according to the phase difference. The total current, which equals zero at each complete cycle, is often referred to as Josephson vortices. For an arbitrary rectangular junction, the current flowing through it at a given flux Φ is given by:

$$I_m(B) = I_c(B = 0) \left| \frac{\sin(\pi\Phi/\Phi_0)}{\pi\Phi/\Phi_0} \right| \tag{9}$$

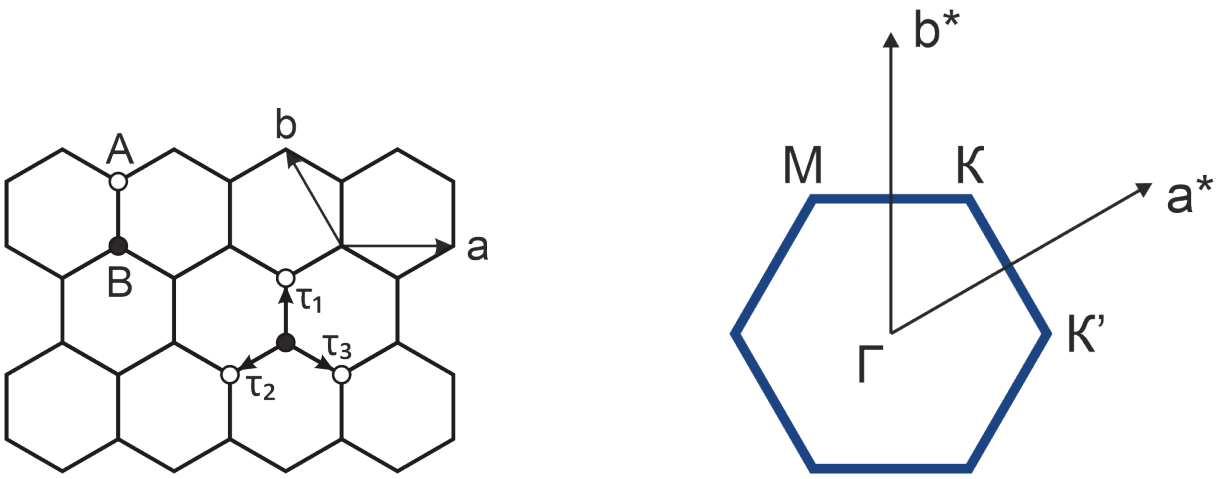

Figure 4: (a): The lattice structure of graphene. **a** and **b** are two primitive translation vectors. τ_1, τ_2, τ_3 are vectors from the B site to the nearest A sites. (b): The first Brillouin zone. Figure a is adapted from [20]

This formula is similar to one for single-slit diffraction in optics and, hence, is usually referred to as the Fraunhofer pattern. The application of Josephson junctions of different geometries has shed light on the nature of high-T_c unconventional superconductors and explored the anisotropy of their wavefunctions[13]. The main geometry used in this work is a rectangular Josephson junction with a weak link made of graphene, the key physics of which is discussed in the next chapter.

2.2 Graphene

2.2.1 Single layer graphene band structure

Graphene is a 2D crystal consisting of carbon atoms assembled into a hexagonal lattice. The lattice structure of graphene and the first Brillouin zone are depicted in Fig. 4. The unit cell includes two carbon atoms at A and B sites and is described by primitive lattice vectors $\mathbf{a} = a(1,0)$ and $\mathbf{b} = a\left(-\frac{1}{2}, \frac{\sqrt{3}}{2}\right)$, where a is the graphene lattice constant, which approximately equals 0.246 nm[21]. The vectors from the A site to the three nearest B sites are defined as $\boldsymbol{\tau}_1 = a\left(0, \frac{1}{\sqrt{3}}\right)$, $\boldsymbol{\tau}_2 = a\left(-\frac{1}{2}, -\frac{\sqrt{3}}{2}\right)$, and $\boldsymbol{\tau}_3 = a\left(-\frac{1}{2}, \frac{\sqrt{3}}{2}\right)$.

Since each graphene atom possesses four valence electrons, three of which form tight in-plane σ-bonds with neighboring atoms, leaving one electron in the $2P_z$ state, only the latter is considered to play a role in conductivity due to its weaker π-bond. The reciprocal lattice vectors are $\mathbf{a}^* = \frac{2\pi}{a}\left(1, \frac{1}{\sqrt{3}}\right)$ and $\mathbf{b}^* = \frac{2\pi}{a}\left(0, \frac{2}{\sqrt{3}}\right)$. The Brillouin zone contains two nonequivalent corners $K = \frac{2\pi}{a}\left(\frac{1}{3}, \frac{1}{\sqrt{3}}\right)$ and $K' = \frac{2\pi}{a}\left(0, \frac{2}{\sqrt{3}}\right)$.

Taking stated the above into account, we can estimate the low-energy band structure of graphene by deriving an effective Hamiltonian within a tight-binding model for π-bond electrons. In the model, the wavefunction can be written down in the following form:

$$\psi(\mathbf{r}) = \sum_{\mathbf{R}_A} \psi_A(\mathbf{R}_A)\,\phi(\mathbf{r}-\mathbf{R}_A) + \sum_{\mathbf{R}_B} \psi_B(\mathbf{R}_B)\,\phi(\mathbf{r}-\mathbf{R}_B), \tag{10}$$

where $\mathbf{R}_A = n_a\mathbf{a} + n_b\mathbf{b} + \boldsymbol{\tau}_l$ and $\mathbf{R}_B = n_a\mathbf{a} + n_b\mathbf{b}$ are coordinates of A and B sites, respectively. The Hamiltonian is given by

$$H = -\gamma_0 \sum_{\mathbf{R}_A} \sum_{l=1}^{3} |\mathbf{R}_A - \boldsymbol{\tau}_l\rangle \langle \mathbf{R}_A| + \text{ h.c. }, \tag{11}$$

where γ_0 is the transfer integral, and $|\mathbf{R}\rangle$ stands for the wavefunction at atomic site $\mathbf{R}$. The Schrödinger equation is then

$$\varepsilon\psi_A(\mathbf{R}_A) = -\gamma_0 \sum_{l=1}^{3} \psi_B(\mathbf{R}_A - \boldsymbol{\tau}_l) \tag{12}$$

$$\varepsilon\psi_B(\mathbf{R}_B) = -\gamma_0 \sum_{l=1}^{3} \psi_A(\mathbf{R}_B + \boldsymbol{\tau}_l). \tag{13}$$

After applying the Bloch theorem the Schrödinger equation takes the form

$$\begin{pmatrix} 0 & h(\mathbf{k}) \\ h(\mathbf{k})^* & 0 \end{pmatrix} \begin{pmatrix} f_A(\mathbf{k}) \\ f_B(\mathbf{k}) \end{pmatrix} = \varepsilon \begin{pmatrix} f_A(\mathbf{k}) \\ f_B(\mathbf{k}) \end{pmatrix} \tag{14}$$

$$h(\mathbf{k}) = -\gamma_0 \sum_{l=1}^{3} \exp(i\mathbf{k}\cdot\boldsymbol{\tau}_l) \tag{15}$$

with the eigenenergies

$$\varepsilon_\pm = \pm\sqrt{1 + 4\cos(\frac{ak_x}{2})\cos(\frac{\sqrt{3}ak_y}{2}) + 4\cos^2(\frac{ak_x}{2})}, \tag{16}$$

where ε_+ and ε_- stand for energies in the conduction and valence bands. The equation represents a valence/conduction symmetric spectrum with the two bands touching at K and K' points at zero energy. By examining the system in the vicinity of these two points of interest, we approximate the energy dispersion relation up to a linear form:

$$\varepsilon_\pm = \pm\hbar v_F |\mathbf{k}| \tag{17}$$

where $\mathbf{k}$ is a wave vector measured from K and K', and v_F is an effective Fermi velocity $v_F = \frac{\sqrt{3}}{2}\frac{a\gamma_0}{\hbar}$.

The low-energy electronic states are expressed in terms of the K and K' points, where wavefunctions are products of plane waves associated with K and K' and slowly (compared to the atomic scale) varying envelope functions

$$\psi_A(\mathbf{R}_A) = e^{i\mathbf{K}\cdot\mathbf{R}_A} F_A^{\mathrm{K}}(\mathbf{R}_A) + e^{i\mathbf{K}'\cdot\mathbf{R}_A} F_A^{\mathrm{K}'}(\mathbf{R}_A) \tag{18}$$

$$\psi_B(\mathbf{R}_B) = -\omega e^{i\mathbf{K}\cdot\mathbf{R}_B} F_B^{\mathrm{K}}(\mathbf{R}_B) + e^{i\mathbf{K}'\cdot\mathbf{R}_B} F_B^{\mathrm{K}'}(\mathbf{R}_B), \tag{19}$$

where $\omega = \exp(2\pi i/3)$ is added to simplify the final equations. After putting these expressions at Schrodinger equations and using long-wave approximation we obtain

$$\mathcal{H}^{\mathrm{K}}\mathbf{F}^{\mathrm{K}} = \varepsilon\mathbf{F}^{\mathrm{K}}, \quad \mathcal{H}^{\mathrm{K}'}\mathbf{F}^{\mathrm{K}'} = \varepsilon\mathbf{F}^{\mathrm{K}'}, \tag{20}$$

where

$$\mathcal{H}^{\mathrm{K}} = \begin{pmatrix} 0 & vp_- \\ vp_+ & 0 \end{pmatrix}, \quad \mathcal{H}^{\mathrm{K}'} = \begin{pmatrix} 0 & vp_+ \\ vp_- & 0 \end{pmatrix}, \tag{21}$$

$$\mathbf{F}^{\mathrm{K}} = \begin{pmatrix} F_A^{\mathrm{K}}(\mathbf{r}) \\ F_B^{\mathrm{K}}(\mathbf{r}) \end{pmatrix}, \quad \mathbf{F}^{\mathrm{K}'} = \begin{pmatrix} F_A^{\mathrm{K}'}(\mathbf{r}) \\ F_B^{\mathrm{K}'}(\mathbf{r}) \end{pmatrix}. \tag{22}$$

The effective Hamiltonians H_K and $H_{K'}$ give the same eigenenergies:

$$H_K = \hbar v_F \mathbf{k}\cdot\boldsymbol{\sigma}, \quad H_{K'} = \hbar v_F \mathbf{k}\cdot\boldsymbol{\sigma}^*.$$

where $p = \sqrt{p_x^2 + p_y^2}$. The effective Hamiltonians presented above are analogous to the Dirac Hamiltonian for zero-mass particles, with linear dispersion occurring at the K and K' points. Hence, graphene presents a valuable platform where one can investigate the behavior of relativistic charge carriers, both electrons and holes, depending on the applied electric field [22].

An important distinction, however, is that instead of real spin, graphene features a valley pseudospin, originating from the equivalency of A and B points of the graphene unit cell. Adding up the degeneracy of the real spin to the effect of valley pseudospin, we have a total of 4-fold degeneracy for the graphene system.

2.2.2 Band gap formation in hexagonal lattice

Now, we will see what happens to the system when introducing asymmetry between A and B sites. In this case, the Hamiltonian takes the following form:

$$\mathcal{H}^{\mathrm{K}} = \begin{pmatrix} \Delta & vp_- \\ vp_+ & -\Delta \end{pmatrix}. \tag{23}$$

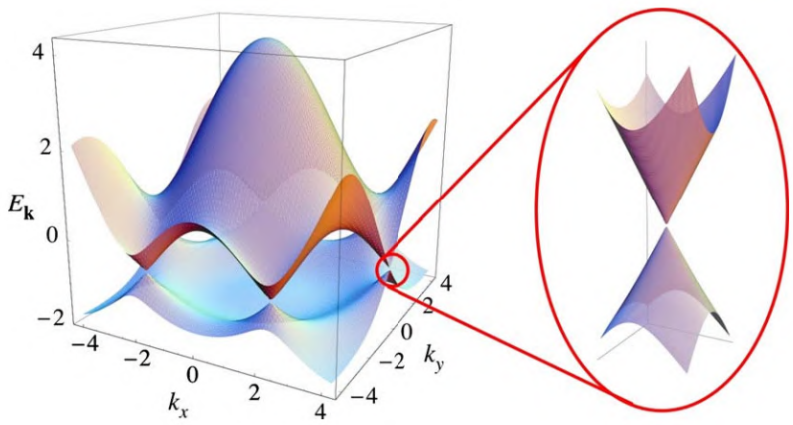

Figure 5: Dispersion relation for graphene. Figure taken from [23].

Now, the Hamiltonian transforms into the one equivalent to the representation of a massive Dirac electron, where Δ and $-\Delta$ terms in the matrix represent an opened energy gap at the Dirac points. As the updated Hamiltonian is no longer invariant under the coordinate inversion operation, one can conclude that the Dirac cones are protected by C_2 symmetry.

The presented explanation is important for understanding the nature of the Dirac cone in graphene and presence of an energy gaps in other 2D materials, such as hexagonal boron nitride (hBN), which has a hexagonal structure with Boron and Nitrogen atoms on A and B sites, respectively. It also illustrates how hBN affects the graphene band structure in layered systems [10].

2.2.3 hBN/graphene structures

The significant interest in hBN/graphene structures stemmed from the marked improvement in graphene quality[24]. While graphene on SiO_2 substrate devices allowed for the first time to observe key features of graphene band structure[25], the overall quality of the devices left a lot to be desired. Substrate roughness[26–28] and scattering from charged surface states and impurities[29–32] were primary limiting factors. These issues led to a significant reduction of carrier mobility away from the one predicted theoretically, and the breakup of the 2D gas into a randomly distributed set of electron and hole puddles near the charge neutrality point[31–33]. hBN encapsulation of graphene was found to significantly reduce the influence of these effects on graphene structure, dramatically improving the quality of the devices[24]. However, the influence of hBN is not limited just to preserving the pure physical properties of graphene when one starts to consider hBN/graphene systems with aligned lattices.

When two periodic 2D structures are overlaid with a twist angle or lattice mismatch, a periodic pattern called a moiré lattice emerges[34]. The periodicity of the moiré pattern for the graphene/hBN structure is characterized by the moiré wavelength λ_m:

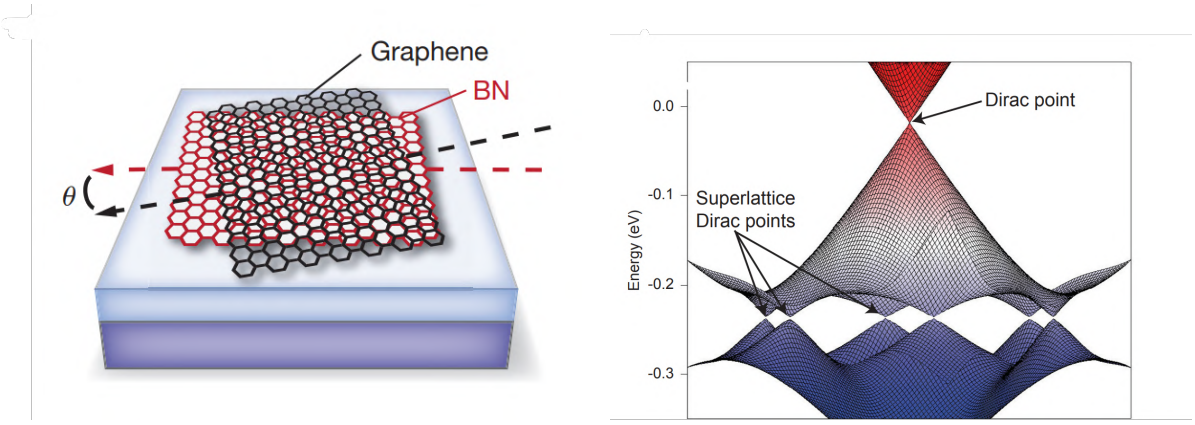

Figure 6: a: Sketch of graphene/hBN structure emerging moire pattern. b: Dispersion relation for graphene aligned to hBN. Figure a taken from [39]. Figure b taken from [38].

$$\lambda_m = \frac{(1+\delta)a}{\sqrt{2(1+\delta)(1-\cos\theta)+\delta^2}} \tag{24}$$

where a is the graphene lattice constant, δ is the lattice mismatch between hBN and graphene, and θ is the twist angle. The effect of the moiré superpotential on the graphene electronic properties can be divided into two components.

Firstly, the moiré superlattice acts on graphene as a weak periodic potential, resulting in the formation of a new set of Dirac points at energies determined by the wavelength of the moiré pattern and hence the rotation angle[35, 36].

Secondly, the increased periodicity in the system significantly alters its behavior under a magnetic field. When a 2D system experiences both a periodic potential and a magnetic field, a recursive energy spectrum, known as the Hofstadter butterfly, can emerge [37, 38]. This effect arises from the interaction between two quantized phenomena: Landau levels generated by the magnetic field and Bloch bands induced by the periodic potential. However, the phenomenon becomes observable only when these two effects occur on a comparable scale. For conventional lattice sizes under one nanometer, extremely large magnetic fields are typically required, making the Hofstadter butterfly challenging to detect. Graphene-based moiré systems are highly effective for observing the phenomenon[39, 40].

3 Experimental Methods

3.1 Fabrication

Fabrication of van der Waals structures with one-dimensional contacts includes the following steps:

1. **Exfoliation**

   We mechanically peel off thin layers of the desired material from the bulk crystal and attach them to a SiO_2 wafer. After that, we examine the wafer with a microscope to select flakes applicable for the next fabrication steps.

2. **Stamp**

   To be able to pick up the flakes of interest we manufacture a stamp consisting of PC and PDMS on the glass stripe.

3. **Stacking**

   We use the fabricated stamp to consequently pick up flakes and construct the van der Waals structure. The completed structure is then transferred from the stamp to a chip with pre-patterned electrodes.

4. **Lithography and contact deposition**

   Finally, we get a complete device after shaping the stack to a certain form using e-beam lithography and attaching one-dimensional contacts by sputtering conducting material.

The process of fabrication used in this work was developed and improved throughout years of research. Starting with the first experimentally achieved thin flakes of graphene and finishing with the development of 1D contact to hBN-encapsulated graphene[24]. For exfoliation, stamp manufacturing, and stacking there were used techniques developed in the[41–44] . In the course of the work on this master thesis project, a significant amount of time was spent developing a recipe for the deposition of a contact material, molybdenum-rhenium (MoRe), on the sample. A detailed description of the fabrication process, including the development of the sputtering recipe, is provided in the chapter.

3.1.1 Exfoliation

The main idea of the exfoliation process widely used nowadays was presented by Geim and Novoselov in 2004 [1]. As the van der Waals force between layers of material is much weaker than chemical bonding, the layers can be detached from one another by use of scotch tape. The process of exfoliation of graphene is the following:

1. We cut a 290 nm thick wafer of SiO_2 into chips of 1 x 1 cm with a diamond cutter. Afterward, we clean the chips with Nitrogen gun to get rid of dust and other physical contaminations and expose them to O_2 plasma to increase adhesion between the SiO_2 surface and graphene flakes. For the plasma cleaning, we use O_2 flow of 50 sccm at power of 25 W. The appropriate duration of the process resulting in good

adhesion is usually from 30 to 60 seconds. Stronger attachment of graphene to the chip may lead to difficulties when trying to pick up the flake from the chip.

2. After that, we take a piece of scotch tape and attach small pieces of bulk crystals to it. Then we fold the piece of scotch tape to thin the material and spread it over a bigger area of the tape. We try to spread the graphene over the surface of the scotch tape with the least amount of folds limiting the number to 5-7 folds. This ensures that the graphite flakes are not severely contaminated with residues of the scotch substrate.
3. We place SiO_2 chips on the scotch tape. To increase the probability of finding good graphene flakes we choose regions on the scotch tape densely covered with mate crystals. The shiny color indicates thicker bulk pieces of graphite. Then we stick the scotch tape with chips attached to it on a glass substrate.
4. We put pressure on the chips manually to increase the adhesion for the flakes and remove air bubbles from the scotch/chip interface if any.
5. After we pressed on the chips for 1-2 minutes we put the scotch tape on a heater of 110°C for 2 minutes.
6. Finally, we can peel the scotch tape off the chips. We need to peel the tape very slowly to ensure that the flakes will not detach from the chip.

The process described above is suitable for exfoliating single-layer graphene flakes. For exfoliating hBN flakes, we use the same approach with few significant differences. For placement of the SiO_2 chip, we look for a rainbowish color on the scotch tape. To pressure the chips, we apply a much weaker force and heat them for a shorter time (approximately 1 minute).

3.1.2 Flake search

After exfoliation is done, we look for the flakes which we will use to stack a device. To find a good graphene flake, we use an optical microscope. Absorption of monolayer graphene is $2,3\%$, and it increases linearly with increasing number of layers. It has been shown experimentally that graphene is most visible on 290 nm SiO_2 substrate [43, 45, 46]. If placed on it, single-layer graphene is visually distinct from few-layer graphene. Generally, we are looking for flakes of monolayer graphene free of scotch residues and not containing areas of thicker graphite flakes. The size of the flake should not exceed 30μm. The use of flakes having the features described above might cause problems during stacking. Residues on the graphene flake will result in an air bubble between graphene and hBN and most probably affect graphene characteristics. Big flakes or flakes with graphite areas are hard to pick up. During the pick-up process, this can result in ripping off the graphene and its folding. In the Fig. 7, there are examples of graphene flakes that are considered useful and not useful for stacking.

For a search of appropriate hBN flakes, we have a different approach. We use hBN flakes of thickness 10-20 nm. Flakes of such thickness are flexible and robust enough for the stacking process and are relatively easy to detect with a microscope. The color of

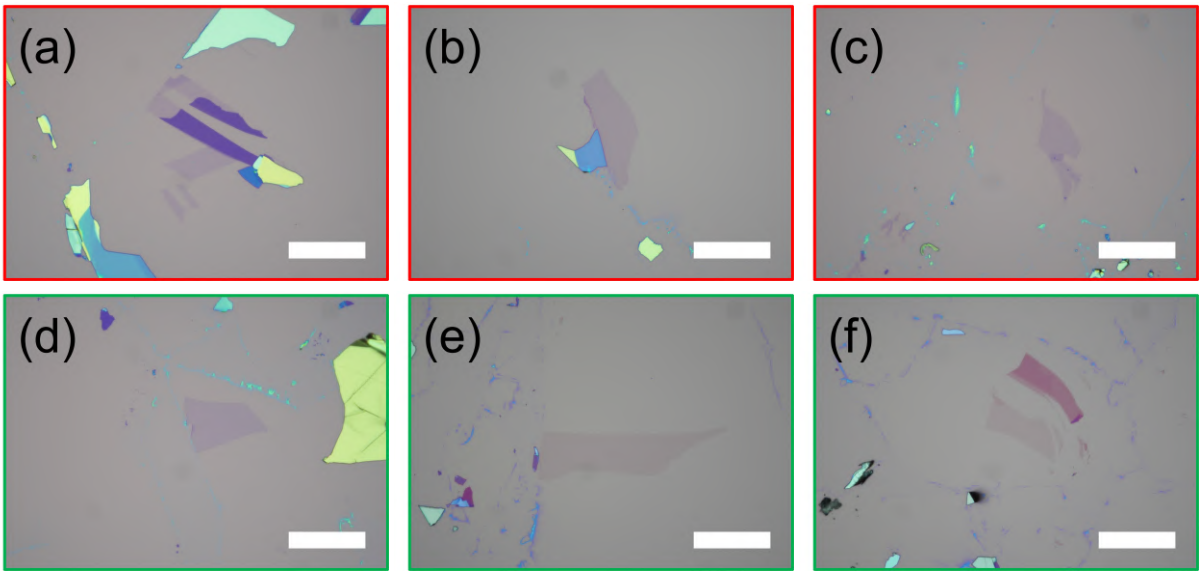

Figure 7: Optical images of graphene flakes. (a) - (c): Images of the flakes not preferable for use. Flakes (a) and (b) are attached to much thicker layers of graphite, while (c) has some residues on it. (d) - (f): Images of flakes considered good for stacking. Scale bar in all the images is 50μm.

the flake visible through the microscope strongly depends on the thickness of the flake, starting from light blue for very thin hBN, going to dark blue and green colors for flakes of medium thickness, and finishing with yellow color for extremely thick flakes. Although one can guess the thickness of a certain flake by the color (e.g., for our purposes, we look for cyan blue flakes), to measure the thickness precisely, AFM scanning of the flake is usually done. As for graphene, we avoid flakes containing different residues. We also aim to use flakes without any cracks on them and of the same thickness throughout the whole flake area. As the color of the flake changes gradually with thickness, some changes in the number of layers in a frame of one flake are sometimes hard to detect. For this reason, observing the flakes with reduced aperture is useful. In the Fig. 8b and Fig. 8c, the same flake is seen through a microscope in different aperture settings. Despite in the wide aperture the flake looks homogeneous, in the narrow aperture different regions with different numbers of layers are visible.

To stack a device with a specific alignment of two different layers of material relatively to each other, one has to have a clue about their initial lattice misalignment. For bilayer graphene devices the issue is usually solved by taking one big flake of graphene and cutting it with AFM tip or laser. The two pieces of graphene have primitive translation vectors aligned parallelly. Later, during stacking, the flakes can be rotated relatively to each other on the angle of choice (for example, on magic angle $\sim 1.1°$). In the case when we want to align hBN and graphene flakes, a different approach is needed. For this purpose, we look for flakes with clear straight edges and a certain angle between them $(30°, 60°, 90°, 120°, 150°)$. As both hBN and graphene have the same hexagonal crystallographic structure except for the slight natural lattice constant difference ($\sim 1.8\%$), the configuration with such angles between two straight edges signifies the existence of zigzag

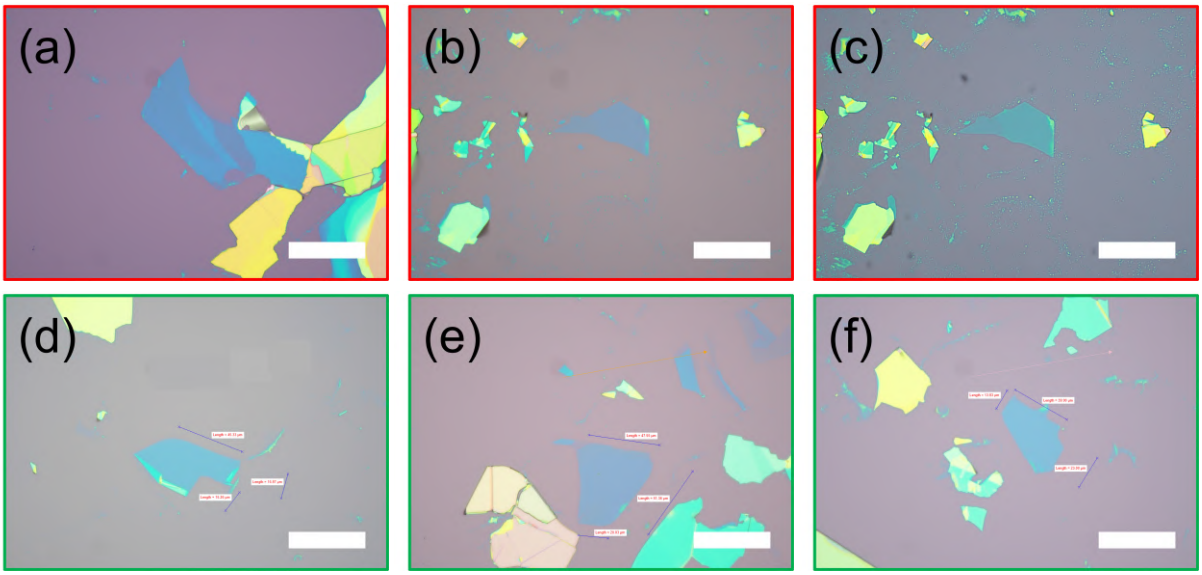

Figure 8: Optical images of hBN flakes. (a) - (c): Images of the flakes not preferable for use. Images (b) and (c) correspond to the same flake, but the image is taken at different apperture settings. (d) - (f): Images of flakes considered good for stacking. Scale bar in all the images is $50\mu m$.

and the armchair edges. Using that information, one can stack an aligned sample by aligning the straight edges of graphene and hBN.

Once a set of good flakes is determined, we proceed to the next step of fabrication.

3.1.3 Stamp preparation

A stamp is a set of transparent sticky polymers placed on a glass slide. The polymers for the stamps used in this work are polycarbonate(PC) and polydimethylsiloxane(PDMS). For the stamp fabrication, we use commercially available PDMS of thickness $\sim$ 1mm. To create a layer of PC we spill a few drops of 5% PC solution on a clean glass slide, place another one on top, and slide them in opposite directions. Afterward, the two slides with a thin layer of PC on them are put on a hot plate of $90°C - 100°C$ for 5 minutes. The process of fabricating the PC slides is complete. Now we have to visually check their quality. A good PC slide has no wrinkles and is fully transparent without any rainbowish colors on it. Once we have thin PC films, we can start fabrication of the stamp.

1. We stick a piece of scotch tape to a clean glass slide and cut out a small square of 1 x 1 cm.
2. Cut out a small square of PDMS (0.5 x 0.5 cm), remove the plastic cover, and place it on another glass slide $\sim$ 0.5cm from the edges.
3. Take one of the slides with PC and cut out a small region (but bigger than a square we cut in the scotch tape) of PC film with a sharp knife avoiding curling and folding of the PC film.

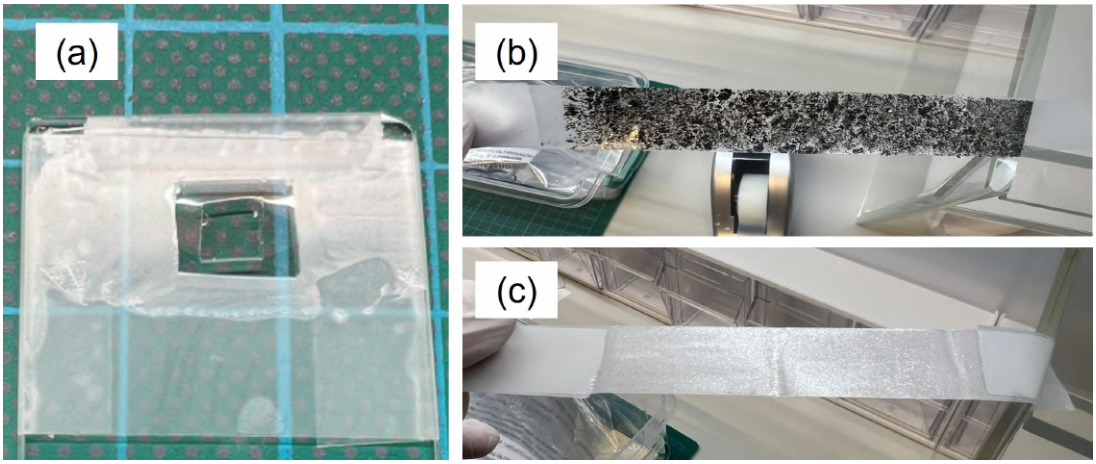

Figure 9: Exfoliation process. (a): Picture of a stamp. (b): Scotch tape covered with graphene crystals. (c): Scotch tape covered with hBN crystals.

4. Take a scotch tape with a square hole, place it on the region of the PC film, and slowly peel it off. We should obtain a free area of PC film suspended by the scotch tape.
5. We stick the tape to the glass slide with PDMS on it, such that the free region of the PC covers the PDMS.

The stamp now is complete. Now we make sure that the PC/PDMS surface is free of air bubbles and inhomogeneities and proceed to the stacking process.

3.1.4 Stacking

The stacking process is done on a transfer stage which allows the assembly of different 2D layers controlling the relative angle between them. The transfer stage is shown in Fig. 10. Its main components are as follows:

1. Vibration reduction stage
2. Sample stage, which consists of the following parts:
   (a) Sample plate. It contains a heater and a temperature sensor to control the temperature of the sample. In the center of the plate, there is a vacuum hole for fixing the position of the substrates with flakes.
   (b) Coarse and fine screws for rotating the stage.
3. The stage position manipulator for moving the stage in X-Y directions.
4. Stamp holder. It consists of the following parts:
   (a) The stamp leg. It contains two vacuum lines to attach the glass slide with a stamp to the leg and to attach the leg to the rest of the stamp holder.
   (b) Screws to move the stamp holder in X and Y directions.

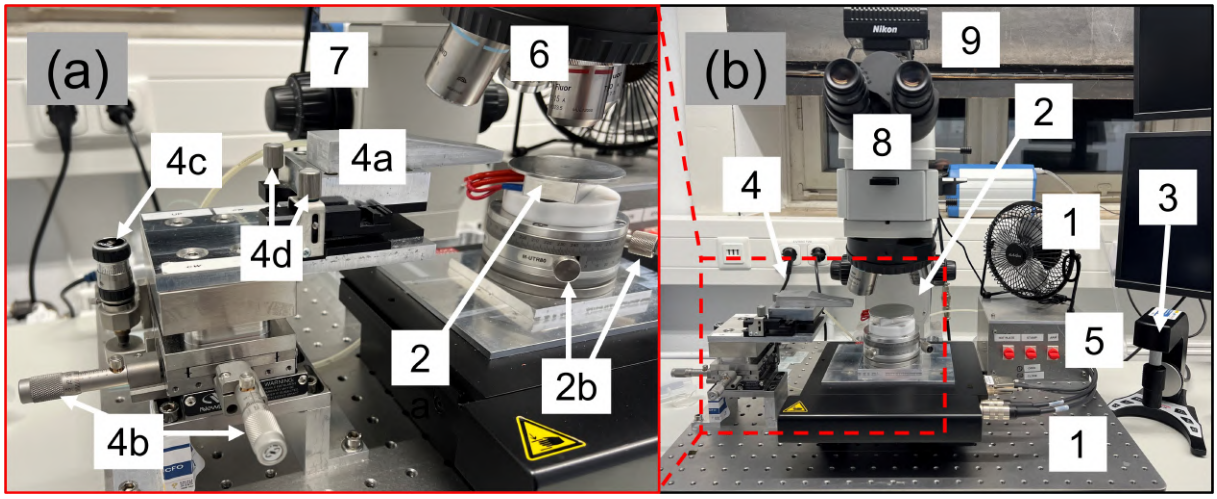

Figure 10: Transfer stage. (a): zoomed in picture of the sample stage and stamp holder. (b): the full picture of the transfer stage set-up. Red dashed lines indicate the sample stage and stamp holder shown in (a).

(c) Screw to move the stamp holder in Z direction.

(d) Screw to manipulate the angle of the stamp leg relatively to the sample stage.

5. Knobs to turn on and off vacuum for sample stage and stamp stage.
6. Microscope with different far-field lenses of magnification 5X, 10X, 20X, and 50X.
7. Focusing knob
8. Eye-piece
9. Digital camera connected to PC
10. Fan for fast cooling of the transfer stage

The process of stacking on the transfer stage is the following:

1. We select a graphene flake and two hBN flakes for the top and bottom layers. The hBN flakes should be bigger than the graphene flake to encapsulate it fully.
2. Then we place a chip with the top hBN layer on the transfer stage and turn on the transfer stage vacuum by turning the according knob.
3. We attach the stamp to the stamp leg and turn on two vacuum lines for the stamp holder. With the screws, we tilt the stamp for a small angle. With screws and manipulators, we locate the PDMS area and the chip underneath the lenses of the microscope. By changing the focus of the microscope we first focus on the surface of PC to find a clean area on it to locate it in the center of the objective. Then we find a chosen hBN flake on the chip and locate it in the center as well.
4. After that, we set the temperature of the sample stage to 110°C and slowly bring the stamp down with the according screws. When the temperature of the sample stage

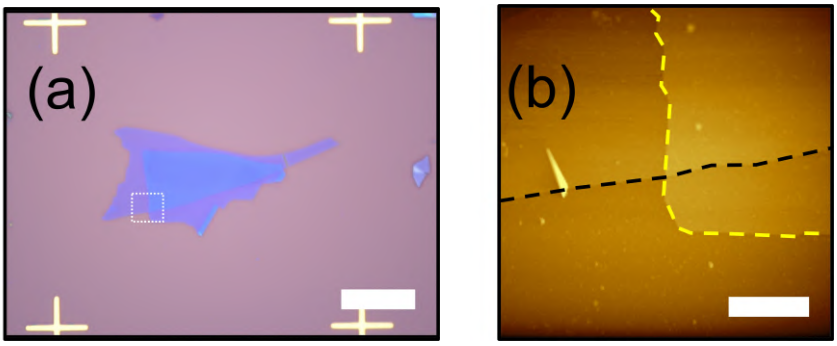

Figure 11: (a): Image of the stack on the pre-patched chip. White dashed line indicates the region where AFM image shown in (b) was done. The scale bar is 25μm. (b): The black and yellow dashed lines indicate the borders of the top and the bottom hBN flakes respectively. The scale bar is 5μm.

reaches 110°C, we can make contact between the chip and the stamp. As the stamp is slightly tilted, the contact first will occur at the edge of the stamp. The area where the stamp and the chip touch will be shown as a "wavefront" propagating along the chip as we slowly bring the stamp lower and lower.

5. We accurately control the Z position of the stamp, letting the wavefront gradually and slowly go through the chip until it fully covers the flake of interest. At this point, it is important not to allow the wavefront to make abrupt jumps. Slow and gradual movement of the wavefront will ensure that we don't fold or crack the flake.

6. After the wavefront completely covers the flake, we wait for 2-3 minutes and slowly lift the stamp allowing the wavefront to slowly go backward.

7. After we ensure no contact between the stamp and the chip, we replace it with a chip with the graphene flake on it. We repeat the process of attaching the flake to the stamp. Now, we ensure that the graphene flake is fully covered with the top hBN flake. If needed, we can rotate the sample stage with the screws.

8. After the graphene flake is picked up, we once again lift the stamp and replace the chip with the one with the bottom hBN flake on it. We once again repeat the procedure ensuring that the bottom hBN flake fully covers the graphene flake as well.

9. Next, we change the chip for the pre-patterned substrate with electrical contacts on it. With the microscope, we look for the location on the chip where we want to fit our sample and place it below the sample.

10. Once again, we slowly make contact between the stamp and the chip. After that, we set the temperature of the sample stage to 180°C. As the temperature slowly increases, at around 140°C – 150°C, the PC will start to melt. On the microscope, one can see the PC detaching from the PDMS surface. Once the temperature reaches 170-180 degrees, we can fully lift the stamp up, leaving the sample on the chip.

11. We turn off the heating and let the chip cool down for several minutes. After that

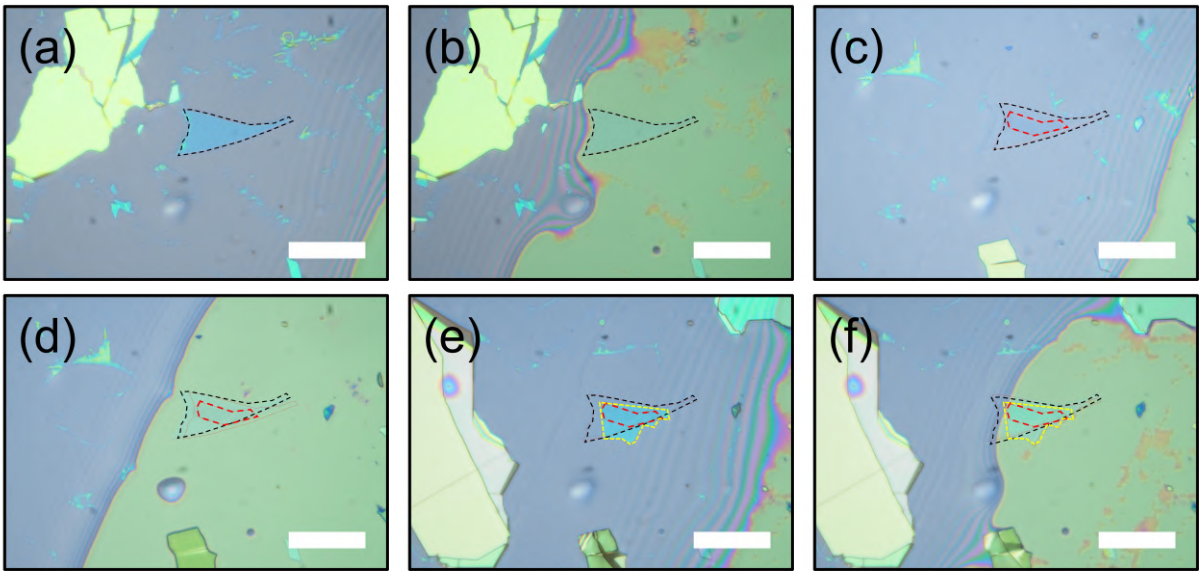

Figure 12: (a) - (f): Process of vertical assembly of hBN encapsulated single layer graphene. The black and yellow dashed lines indicate the top and the bottom hBN layers respectively. The red dashed line indicates the graphene flake. Green area shows PC wavefront spreading through the surface. Scale bar in all the images is 50μm.

we clean the chip from the PC residues by putting it in dichloromethane (DCM) for 5 minutes and IPA for 2 minutes.

After the stacking is complete, we switch to the lithography process to shape the stack into a certain geometry with reactive-ion etching and make electric contacts via sputtering.

3.2 E-beam lithography

The next step of fabrication is creating a photoresist mask which we expose to e-beam lithography. Next, we etch the chip in the reactive ion etcher (RIE) and clean the chip from the photoresist. To make electric contacts we once again repeat the procedure but sputter electric contacts right after etching.

1. We start the process by creating the design of the sample in KLayout. Here we define the shape of the future JJs.
2. Then we create a photoresist mask by spincoating PMMA 950K in a spincoater at 6000 rpm for 40 seconds with the following baking at 150°C for 2 minutes. This will give a layer of PMMA of approximately 300nm.
3. After that, we do e-beam lithography. For such thickness of PMMA and device sizes we use step of 8nm, and area dose of 100μC/cm^2.

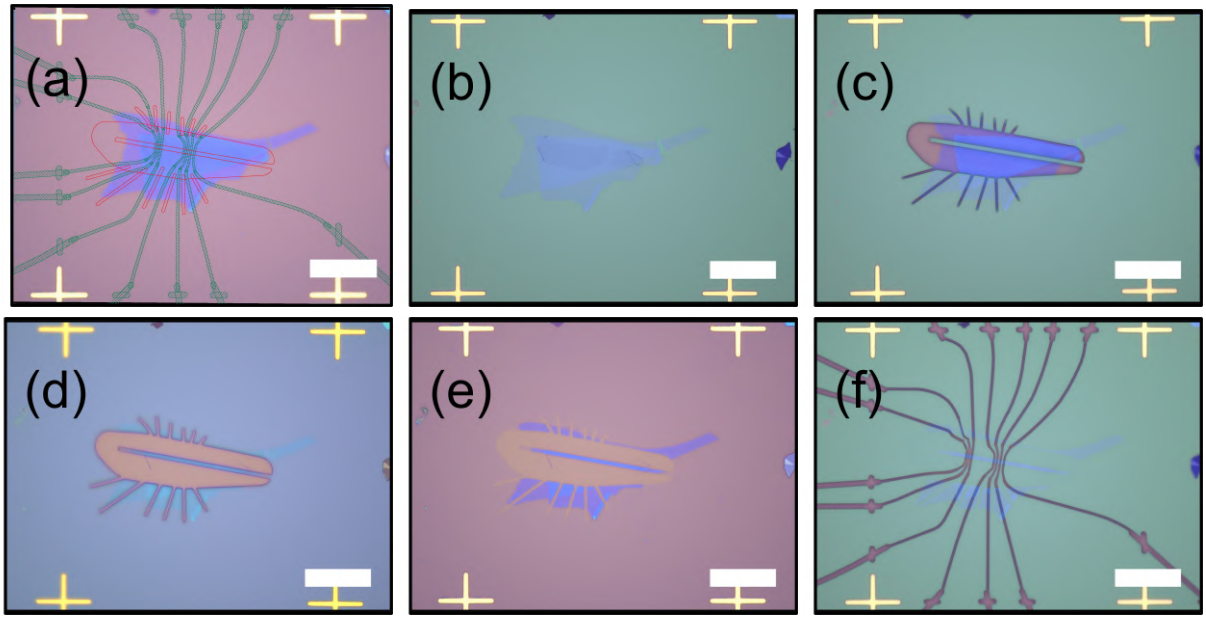

Figure 13: (a) - (f): Images of the stack during fabrication process. Scale bar in all the images is 50μm.

3.3 Photoresist development and etching

1. We develop the photoresist in a solution of IPA and DIW (7:3) at room temperature for 1 minute 20 seconds. After that, we proceed to etching at RIE with a combination of gases CHF_3 and O_2 (the flow rate is 40 and 4 sccm respectively) at generator power 20W. The procedure is done when all hBN and graphene in the exposed area is completely etched.

2. After that, we design the electric contacts to the graphene in Klayout to do spin-coating and e-beam lithography once again. The electric contact design should not contain sharp corners or abrupt curves. Such design features cause the formation of cracks and wrinkles on the surface of the conducting material. As the characteristic scale for our samples reaches 0.25μm the formed inhomogeneities are enough to strongly affect the sample (e.g., short the neighboring contacts).

3. Now we proceed to etching. The etching recipe described above yields the etching rate for hBN 19nm/s and 1.6nm/s for graphene. Such a relation of etching rates is considered good for the quality of 1D contacts to graphene. Knowing the thickness of the top and bottom hBN, we estimate the duration of etching required to etch through the flakes.

After the etching is done, we immediately take the sample and put it into the vacuum chamber for the following sputtering. This is done to minimize the exposure of the clean 1D graphene surface to the air.

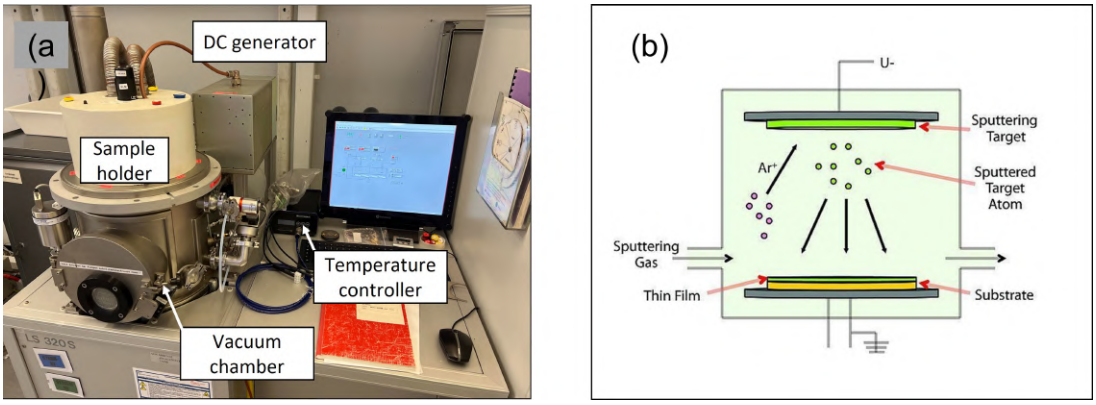

Figure 14: (a): Picture of the sputtering system. (b): Schematic diagram illustrating the concept of the sputtering process. Figure b taken from [47].

3.4 Sputtering and recipe development

Sputtering is a process of depositing thin films. The process is described in Fig. 14b. Plasma gas (in our case Ar) is ignited and accelerated by a DC power supply to collide with the surface of a target material and detach particles from it. Afterwards, the particles homogeniously cover the substrate. The properties of the deposited thin films (such as superconductivity, resistance, Tc, and film thickness) strongly depend on how the sputtering is done. In our case, requirements for good quality contacts to graphene, preservation of high Tc, homogeneity of the MoRe film, and precise geometry of contacts after lift-off caused a challenge in finding the right settings for the sputtering process. The main issues faced along the way and the algorithm used to solve them will be described below.

The sputtering occurs in the sputtering machine "Von Ardenne LS 320 S" (Fig. 14a). The vacuum chamber capable of vacuums below 10^{-6}mbar contains a target carousel with 6 sample positions, 1 DC generator, and 2 RF sources. Argon is injected into the chamber. The flow of Argon is measured with a sensor located in the chamber and can be controlled through a PID loop. The substrate is placed on a sample holder, which in turn is placed in the lower part of the chamber, which is separated from the target holders with a rotating shutter. The sample holder consists of a heating element and thermopair for controlling the sample temperature during the sputtering process. The signal from the thermopair is used to adjust the voltage applied to the heater with the PID loop. The temperature of the sample and the voltage applied to the heater can be seen and controlled through the software. The setup allows the user to set up the temperature of the sample as well as the rates at which the sample is heated and cooled. An example of the change in the temperature of the sample and the voltage applied to the heater during the sputtering process is shown in Fig. 15. As the outcome, we have the following parameters we can tune and control for achieving the film of desired properties: DC voltage, the temperature of the sample holder, Ar flow rate, and the duration time of sputtering.

The most frequent problem met throughout the recipe development for the desired MoRe film was crumpling of the film due to applied temperature stress. As the Ar plasma

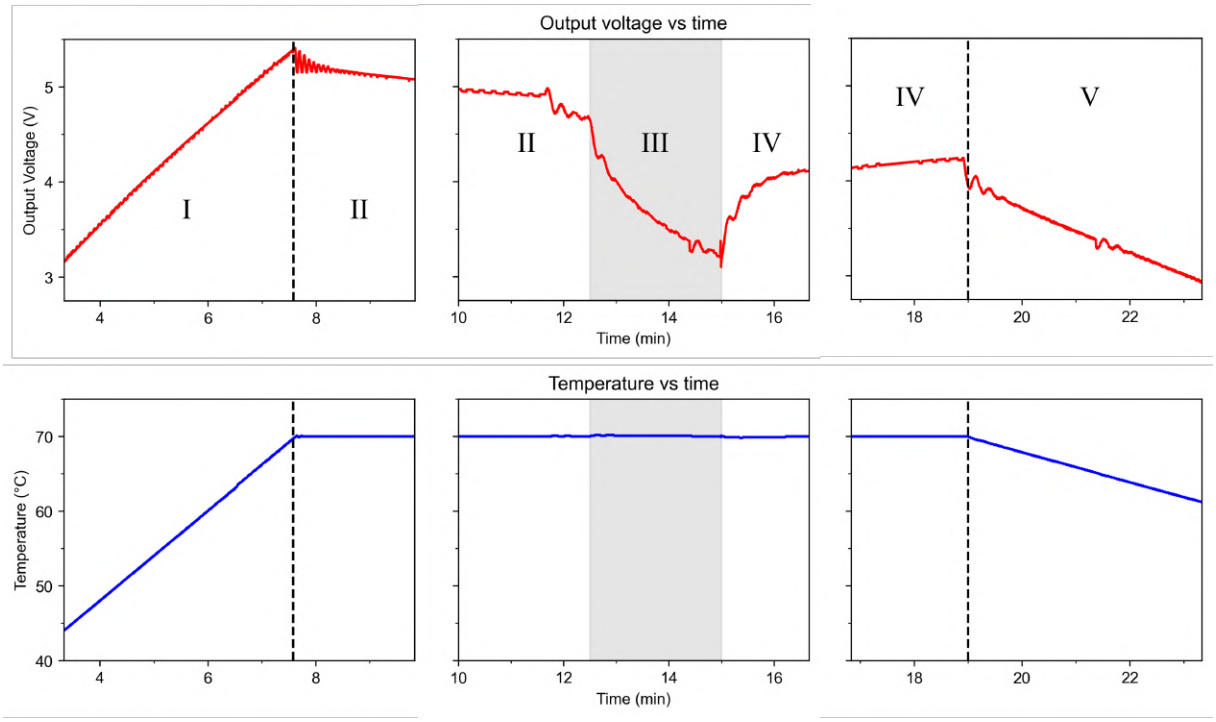

Figure 15: Plot of the voltage applied to the sample holder and temperature of the sample while in the sputtering chamber.I: heating of the sample. II: stabilizing of the temperature of the sample. III: process of sputtering. IV: stabilizing of the temperature of the sample. V: cooling down. Gray area indicates a process of sputtering.

hits the target, it also heats the ejected particles, which in turn heat the substrate. The short-term high thermal stress causes the thermal expansion of PMMA, which affects the MoRe film. To reduce the thermal stress, one can reduce Ar flow or lower the applied DC voltage. This will reduce the amount of target material particles and their kinetic energy which reduces applied thermal stress. However, such a reduction of sputtering rate might affect the film's surface smoothness and purity, hence suspending superconductivity. Reduction of the sputtering time, on the other hand, also leads to minimized thermal expansion but also leads to thinner MoRe film. At some point, good electric contact between thin MoRe electrodes and graphene exhibiting an elevated position relative to the substrate can't be assured.

Taking into account stated above, the following protocol was suggested for finding appropriate settings for sputtering:

1. Adjust Ar flow and DC voltage by sputtering MoRe contacts on SiO_2 chips with prepatched golden contacts and checking the superconducting properties of the electrodes. The DC voltage should be reduced but to the values where the sputtered MoRe still shows expected superconducting properties sustainably over several sputtering session.

2. Estimate the sputtering rate with the found parameters using AFM for measuring MoRe thickness and calculate the time needed for achieving thickness required for

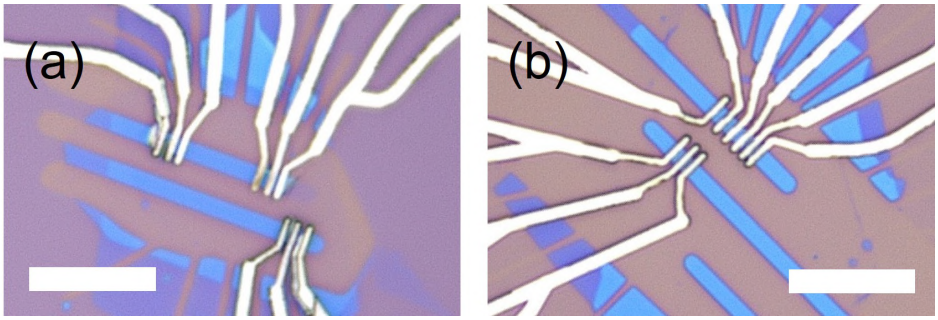

Figure 16: Images of two devices after the complete fabrication process. (a): Image of a not working sample after a bad sputtering process. (b): Image of a working sample after the sputtering process described in the text. The scale bar is 10μm.

good MoRe/graphene contact. With the bottom hBN being lower than 20nm in our system, we set a benchmark at 50nm for MoRe contacts. At this point, the sputtered film might still suffer from thermal stress. This issue should be resolved in the following step.

3. With the rest of the parameters fixed, we now tune the last one: the temperature of the sample holder. By tuning the temperature settings for the sample heater placed on the holder, we aim to reduce the voltage drop in the current applied to the heater at the start of the sputtering process and, hence, reduce the exposure of the sample to the stress.

4. When all the parameters are modified, we conduct a final check of the sputtering settings. The sputtering procedure should robustly provide a homogeneous film without visible wrinkles and cracks on the surface and on the edges of the contacts received after lift-off. We once again measure the sputtering rate (it should not have significantly changed since the last measurement) and clarify that it allows us to achieve the desired thickness of the MoRe contacts. Finally, we check that the MoRe films transform to a superconducting state at the expected critical temperature.

An important detail: for each sputtering session, a short presputter(sputtering when the sample is covered from target material particles by the shutter) should be done. It is completed to ensure that the surface of the target is cleaned from the oxidized layer.

Following the protocol, these settings for the procedure were found:

1. The sample is controllably heated to 70°C with the heating rate 6°C/min.

2. After the pressure in the chamber is below 10^{-7}mbar, presputtering is done. For that, the DC generator is tuned for 35 W, and the Ar pressure is tuned to be $\sim 3.5e^{-2}$mbar. The presputter session lasts for about 3 minutes.

3. The power of the DC generator is reduced to 30 W, and Ar pressure is changed to $\sim 2.5e^{-3}$mbar.

4. After the Ar pressure and temperature are stabilized, the shutter is rotated to start the sputtering process. After $\sim$ 150 seconds, the process is stopped by rotating the

shutter once again.

5. A Few minutes after sputtering is done, the sample is cooled down with the rate 2°C/min.

As a result, after the sputtering, we obtain a surface of a superconducting thin film of MoRe with almost no cracks or wrinkles uniformly covering the sample. The next step of fabrication is the lift-off. To do it, we place the sample in acetone and keep it at 60°C for several hours. After that, we spray some acetone with a syringe to detach all unwanted metal. While keeping the sample in acetone, we check with the microscope that the lift-off is done (otherwise, we can spray some more acetone) and blow the sample with N_2. This is the last step of the fabrication. In Fig. 16, pictures of two completed devices are shown. Residues on the contacts and their irregular shape in the device (a) are the result of bad sputtering. In contrast, if done correctly, as in Fig. 16b, the contacts to the graphene are much more clear.

After the fabrication is completed, we prepare the sample for the measurements. For this, we glue the chip to the chip carrier with silver paste and wire bond the contacts of the sample with those of the carrier.

4 Results

4.1 Graphene Sample Non-aligned to hBN

4.1.1 Contact Resistance

We start with the basic characterization of the superconducting contacts. AFM measurements of the contacts, fabricated according to the procedure specified in the previous chapter, are presented in Fig. 17(lower inset). The thickness is measured at the interface between the gold pre-patched contacts and the MoRe layer. This approach is necessary because exposure to the etching process can cause the SiO_2 layer to lose some of its uppermost material, leading to an underestimation of the contact thickness if measured directly. Gold, being far less susceptible to etching, offers more reliable results. The measured thickness is approximately 55nm, from which we estimate a sputtering rate of around 22nm/min for the applied recipe.

Resistance measurements conducted on the MoRe electrodes, as shown in Fig. 17, reveal a drop to zero at 8.45K. The corresponding energy gap, calculated using eq(1), is $\sim$ 1.3meV. Both of these values align well with previously reported literature on this type-II superconductor[48–50].

One of the key characteristics that defines the quality of a graphene/metal contact is its resistivity. To measure it, we fabricated a series of Josephson junctions with different lengths but identical widths. The total resistance of the junctions is given by $R = 2R_c + \rho L$, where R_c is the contact resistance, ρ is the linear resistivity of the graphene channel, and L is the junction length. The contact resistance can be extracted from the linear fit of the data as shown in Fig. 19, where the intercept divided by two provides R_c. This method is referred to as the transfer-length method (TLM).

In graphene-based junctions, two different geometries can generally be implemented. The first design (shown in Fig. 18) divides the graphene contacts into two sets of electrodes, enabling 4-probe measurements. This design allows to connect the current source and voltmeter separately to eliminate the influence of the line resistance. However, a challenge arises when the device temperature exceeds the critical temperature of the electrodes. In such case, the measured resistance includes not only the graphene's resistance but also the resistance of the electrode segments. This becomes especially problematic when comparing measurements across different junctions, as the electrode segment resistance may vary between junctions. For this reason, the second design (Fig. 18b) is more suitable, as it minimizes the effect of MoRe resistance, even when the temperature exceeds T_C.

The Fig. 18b shows the set of junctions used for the TLM measurements. Resistance was measured at Si gate voltages between 33 and 37 volts, away from the charge neutrality point (CNP), and averaged over 17 measurement points. The plot of resistance versus junction length is presented in Fig. 19. From the linear fit, the contact resistance is found to be $80 \pm 7\Omega \cdot \mu$m.

A notable disadvantage of the TLM method arises when the junction lengths systematically deviate from their prescribed values, which can be caused by the multi-step

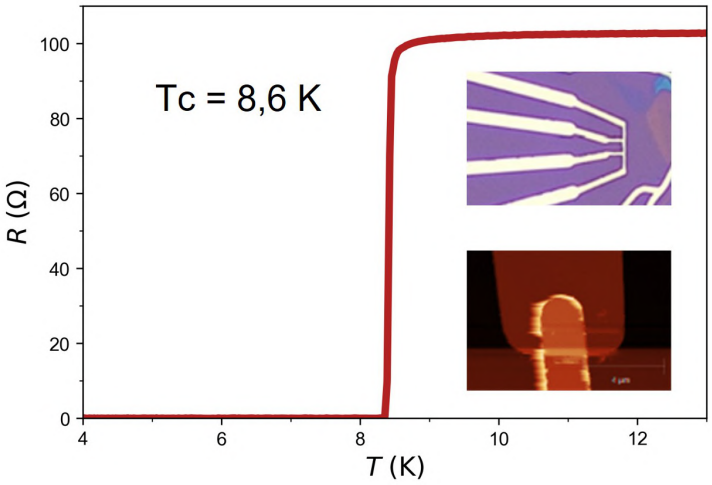

Figure 17: Measurement of the resistance of MoRe contacts as a function of temperature. Upper inset: a picture of the MoRe Hall bar on which the measurement was conducted. Lower inset: an AFM scan of the MoRe contact to the golden pre-patched pattern.

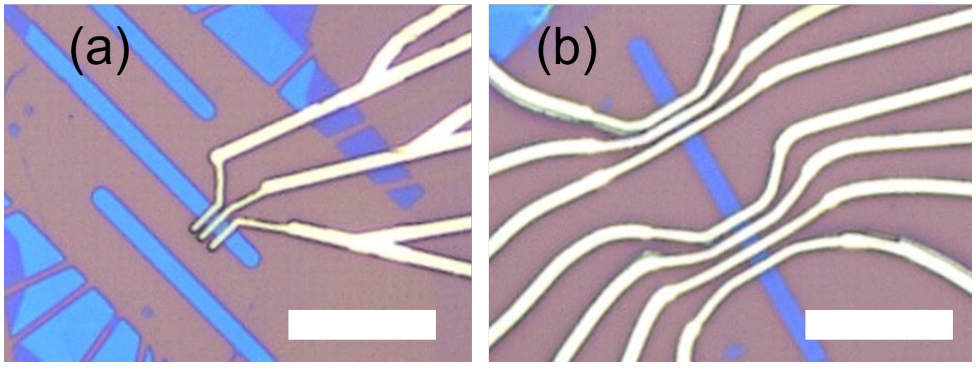

Figure 18: Pictures of two possible designs of the Josephson junctions. Geometry (b) is preferable for the measurements above critical temperature. The scale bar in the images is 10μm.

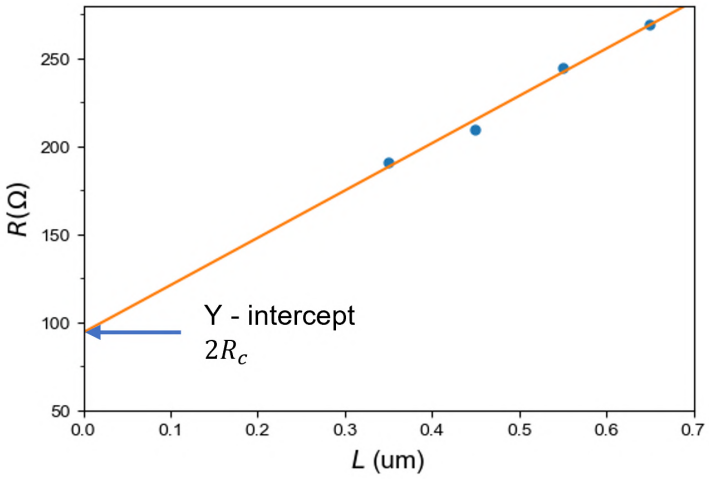

Figure 19: Transfer-length method. Blue dots: values of the resistance of the Josephson junctions as a function of length. Orange line: linear fit of the dependence of the resistance from the length of the junction. The intercept of the fit with vertical axes gives the value of double the contact resistance. The measurements are done at the temperature above the critical temperature of MoRe.

fabrication process. Despite this, the linear relationship between resistance and length may still hold, making it difficult to detect the error. Given this, the actual contact resistance could be slightly higher than the measured value. Even if we assume that all junctions are 0.25 µm shorter—short enough to short one junction—the contact resistance would still be approximately 120 $\Omega \cdot \mu$m, not much bigger than values presented in the literature [24]. Such resistivity value indicates high-quality contacts.

Overall, the sputtering process developed during this master's thesis project has resulted in reliable contacts to graphene, exhibiting stable superconducting properties across various devices.

4.1.2 Basic characterization

Now that the quality of the graphene contacts is ensured, we can proceed with the basic characterization of the single-layer graphene device encapsulated in hBN. We will begin by examining graphene that is not aligned with any of the hBN flakes. In this configuration, the influence of hBN on graphene's behavior is minimized, limiting its effect to the "improved quality" of the graphene, thereby allowing us to observe its "natural" behavior. In this chapter, we will focus on two junctions, JJ1 and JJ2, both with a graphene width of $W = 1.5\mu$m, but with different lengths: 0.3μm for JJ1 and 0.5μm for JJ2.

Fig. 20 displays the resistance measurements of two junctions as a function of the Si gate voltage. The behavior observed is typical for single-layer graphene. The peak in resistance signifies that the Fermi level has reached the Dirac point, at which the resistance sharply increases because, according to the band structure, there are no free charge carriers available. In reality, however, the position of the charge neutrality point

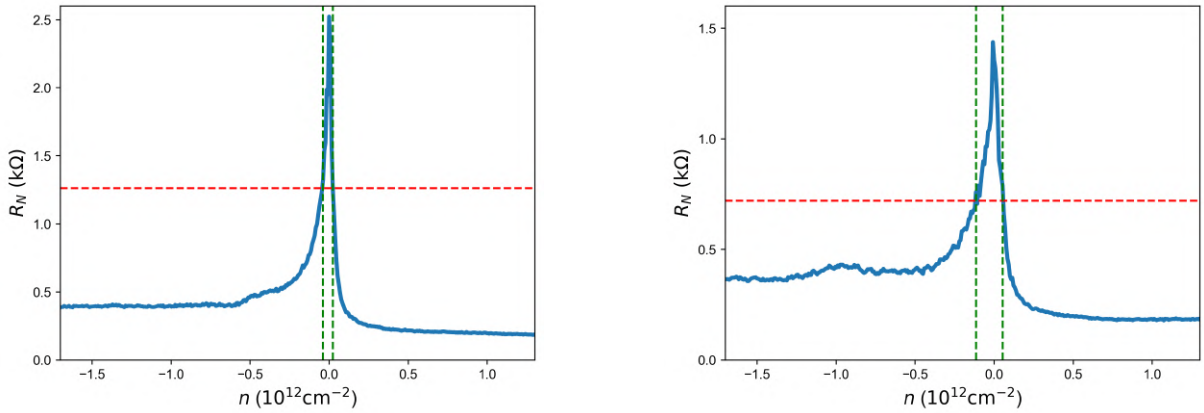

Figure 20: Measurement of the resistance of the junctions as a function of voltage gate. Red dashed line indicates values of resistance equal to half of the maximum value of resistance. The vertical green dashed lines indicate the values in voltage gate where these values were obtained.

shifts energetically across the graphene, resulting in the formation of randomly distributed electron and hole puddles. These puddles lead to an increase in the width of the resistance peak observed in the measurements. Thus, the width of the resistance peak serves as an indicator of charge-carrier inhomogeneity. The full width at half maximum (FWHM) of the resistance peak for the JJ1 is approximately $\delta n \sim 6 \times 10^{10}$ cm^{-2}. This value is consistent with earlier results on similar devices, showing a threefold improvement compared to SiO_2-supported samples [24, 48], but is around six times greater than the widths reported for suspended graphene systems [51]. The existence of these electron-hole puddles has a significant impact on the proximity effect of the system at the charge neutrality point, which will be explored in subsequently.

Another critical factor influencing the physics of graphene is the strong scattering of charge carriers due to impurities. To quantify the impact of these impurities on our sample, we estimate the charge carrier mobility in the graphene by fitting the measurements presented in Fig. 21 to the Boltzmann equation for transport

$$\sigma^{-1} = (\ \mathrm{ne}\ \mu_\mathrm{c} + \sigma_\mathrm{o})^{-1} + \rho_\mathrm{s}, \tag{25}$$

where μ_c is the density-independent mobility caused by charge-impurity Coulomb scattering, ρ_s is the contribution to resistivity from contact resistance and short-range scattering, and σ_0 is the residual conductivity measured at the charge neutrality point (CNP)[24]. Through the fitting procedure, we can estimate the mobilities for the junctions, with $\mu_c \approx 87000$ and $218000\,\mathrm{cm}^2/\mathrm{Vs}$ for JJ1, and $\mu_c \approx 112000$ and $143000\,\mathrm{cm}^2/\mathrm{Vs}$ for the hole and electron sides, respectively. These values align well with those reported for previous graphene/hBN systems[24] and suspended graphene [51]. Additionally, we derive the contact resistance from ρ_s using the formula $R_c = \frac{\rho_s W}{2}$, resulting in contact resistances of $R_{c1} \approx 117\,\Omega$ for JJ1 and $R_{c2} \approx 90\,\Omega$ for JJ2, which approximately matches the values obtained by TLM.

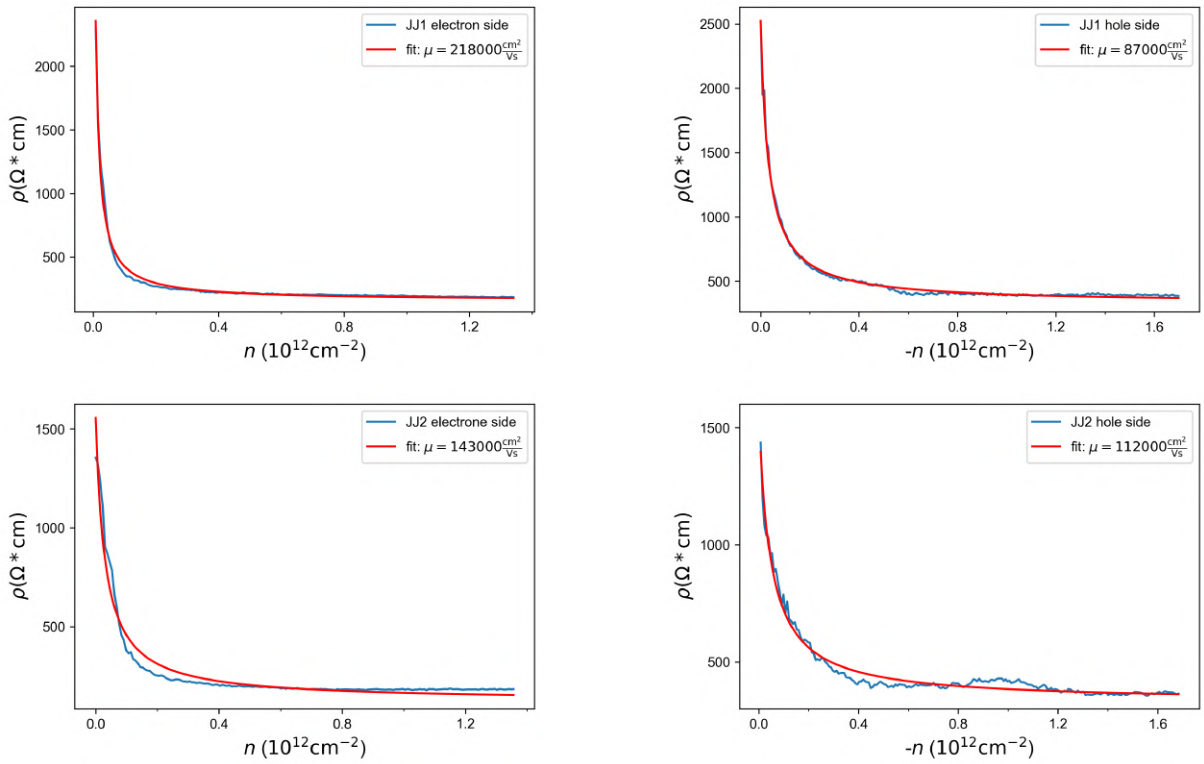

Figure 21: Fit of the Boltzmann equation for the two junctions. The fit is completed separately for electron and hole side for both of the junctions. The approximate value of mobility is shown in the upper right corner of the graphs.

The asymmetry of the resistance values for electron and hole sides, as well as the shift of resistance peak from zero voltage, is explained by n-doping caused by metallic contacts. As the fermi energy is higher for MoRe, the graphene is constantly doped by electron flow from the metal. This effectively increases fermy energy above the CNP, which explains why finite negative gate voltage for reaching the CNP is needed. Furthermore, the doping also causes the formation of an npn junction once the graphene on the hole side, which effectively increases the resistance of the system.

The measurements conducted at the temperature of 300 mK in Kiutra are presented in Fig. 22a. We observe that the resistance on the electron side drops to absolute zero. To further investigate this phenomenon, we conduct differential resistance measurements for this region, as shown in Fig. 22b. We notice a constant value of differential resistance when the applied DC current exceeds ± 1 mA, and drop of the resistance to zero as the current is smaller than ± 1 mA. This behavior is characteristic for superconductors, clearly indicating the proximity effect within the junction.

To further investigate the proximity effect in the system, we conducted the same measurement as shown in Fig. 22b across a range of Gate voltages, producing differential resistance maps displayed in Fig. 23. Superconducting pockets are observed on both the electron and hole sides, separated by the absence of proximity at the charge neutrality

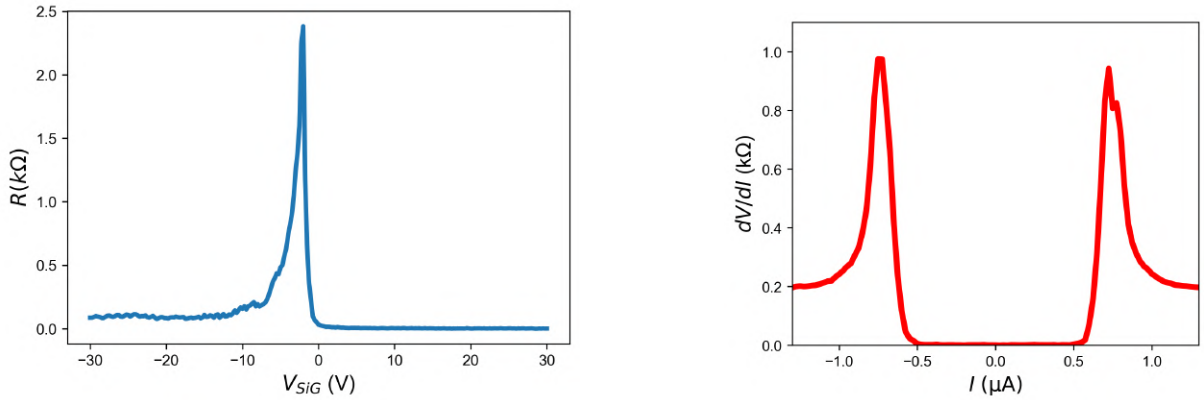

Figure 22: Transport measurement of the Josephson junction at 300mK. (a): measurement of the resistance as a function of the voltage gate. (b): The measurement of the differential resistance completed at electron doping of the graphene.

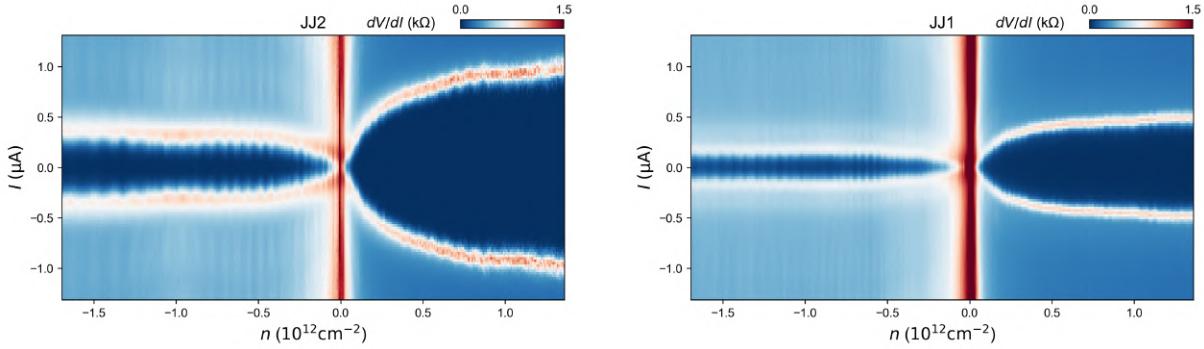

Figure 23: Maps of differential resistance obtained for the junctions.

point (CNP). When comparing the two junctions, we observe that the shorter junction has a generally higher critical current where proximity disappears. This behavior is consistent with the presence of npn junctions stated previously. The creation of these junctions also gives rise to oscillations in both the critical current and normal resistance on the hole side. In the presence of the formed cavity, the transmission probability for charge carriers is reduced, causing the interference of electrons reflecting from the pn interfaces. By altering the gate voltage, the interference shifts between constructive and destructive, leading to Fabry-Pérot (FP) oscillations, similar to optical interferometry. To confirm that these oscillations are indeed due to the FP effect, we plot the points where constructive interference occurs, as shown in Fig. 24. For zero external magnetic field, an expression for the resonance condition is

$$\frac{L_{\mathrm{c}}}{\lambda_{\mathrm{F}}\left(V_{\mathrm{gate}}\right)}=N+\frac{1}{2}, \tag{26}$$

where N is the mode of interference, λ_F is the Fermi wavelength controlled by gate voltage ($\lambda_F \sim \frac{1}{\sqrt{V_{\mathrm{gate}}}}$), and L_c is the reduced cavity length due to the formation of

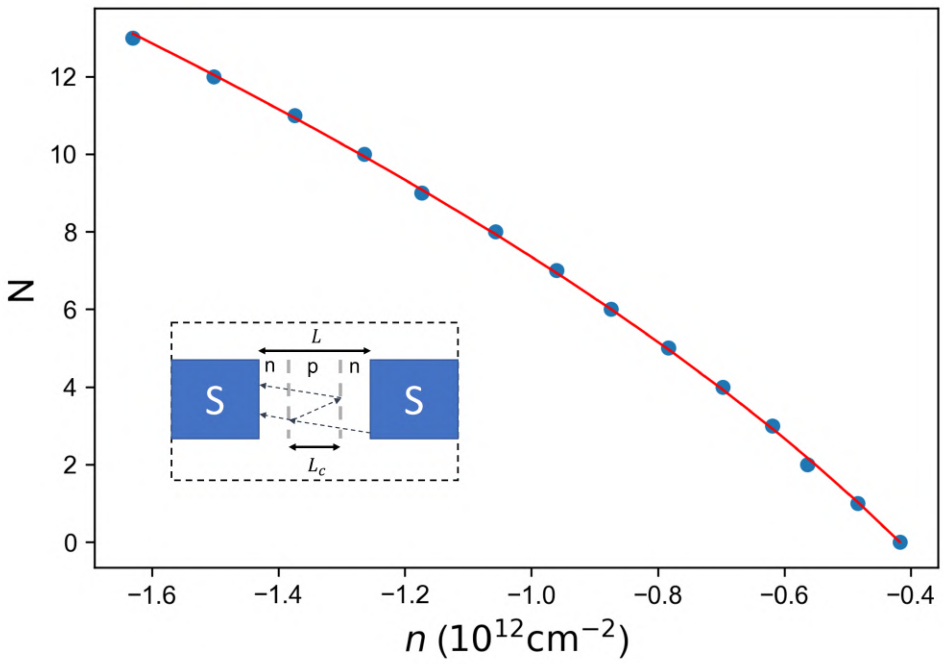

Figure 24: Fabry-Pérot oscillations. Blue dots shows dependence of number of the mode from the charge carrier density. The red line: the square root fit. Inset: the scheme of the formed npn junction and reduced cavity length.

the *npn* junction. From this equation, we observe that the interference mode has a square root dependence on the applied gate voltage, which is exactly what we observe in our measurement. We emphasize that this effect is possible only when charge carriers propagate through the junction ballistically (at least partially).

To investigate further whether the transport at the junctions is ballistic or diffusive, we can take two approaches. The first approach involves considering the Thouless energy, which characterizes the time required for electrons to traverse the junction. In the case of diffusive transport, the Thouless energy is given by the following expression:

$$E_{\mathrm{Th}} = \frac{\hbar D}{L^2}, \tag{27}$$

where L is the length of the junction, and $\hbar$ is the Planck constanta and D is the diffusion constant

$$D = \frac{v_F l_{mfp}}{2}. \tag{28}$$

In a ballistic Josephson junction, where the mean free path is longer than the length of the junction ($l_{mfp} \gg L$), the traversal time can be estimated as $\tau \sim \frac{L}{v_F}$, where v_F is

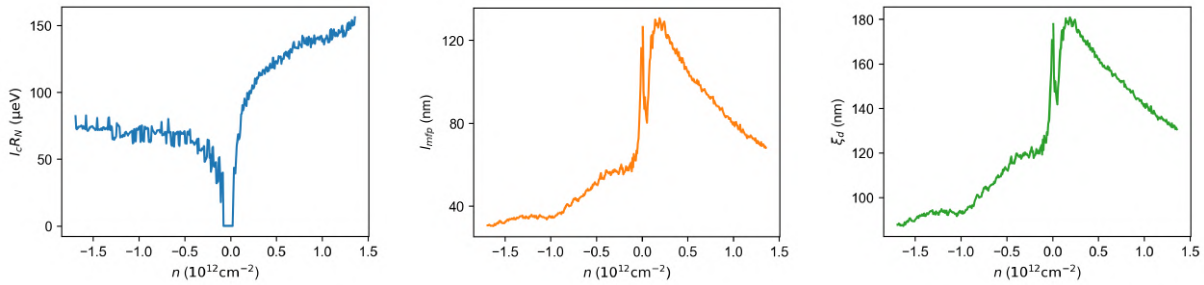

Figure 25: Characterisation of the graphene Josephson junction. (a): product of critical current and normal resistance as a function of carrier density. (b): mean free path of the charge carriers as a function of carrier density. (c): coherence length calculated in a diffusive regime.

the Fermi velocity. Then, the Thouless energy for ballistic transport can be estimated as:

$$E_{\mathrm{Th}}^{\mathrm{ballistic}} = \frac{\hbar v_F}{L} \tag{29}$$

In the diffusive regime, the product of normal resistance and critical current is expected to be proportional to the Thouless energy

$$I_c R_N \sim \frac{E_{\mathrm{Th}}}{e}. \tag{30}$$

However, in the ballistic regime, when the time spent by the electrons in the junctions is limited, the relevant energy scale is superconducting energy gap of MoRe Δ

$$I_c R_N \sim \frac{\Delta}{e}. \tag{31}$$

Another approach is to straightforwardly estimate and compare the mean free path to the length of the junction.

$$l_{mfp} = \frac{\hbar L}{e^2 W R_N} \sqrt{\frac{\pi}{n}} \tag{32}$$

The mean free path and product IcRn for the junctions are presented in Fig. 25a. For both of the junctions the IcRn product is comparable to the energy gap $I_c R_n \approx 0.1\Delta$ The mean free path for the junctions varies from 50 to 200 nm for JJ1 and from 30 to 130nm for JJ2.

In summary, although the mean free path is calculated to be shorter than the junction lengths, the energy scale and FP oscillations point toward ballistic transport. Thus, we

can conclude that the junctions are in an intermediate regime, where some electrons exhibit ballistic behavior as they propagate through the junction.

The next step is to classify the junctions based on the relationship between the junction length and the coherence length, ξ, which represents the characteristic distance over which the superconducting order parameter remains coherent. When the junction length is much smaller than the coherence length, the junction is classified as short; otherwise, it is considered long. In ballistic junctions, the coherence length is determined by the Fermi velocity, while in diffusive junctions, it is related to the diffusion constant D.

$$\xi_b \sim \frac{\hbar v_F}{\Delta} \quad \xi_d \sim \sqrt{\frac{\hbar D}{\Delta}} \tag{33}$$

As our junctions are working in the intermediate regime, the estimation of the coherence length is unclear. For more clarity, we use both of the approaches. The coherence length for the diffusive regime are shown in Fig. 25c. Since the coherence length in the ballistic regime is independent of both carrier density and junction length, we consistently obtain a value of 160 nm. For both junctions, the coherence length is shorter than the junction lengths in both the diffusive and ballistic regimes, indicating that these are long junctions. In long junctions, the superconducting wavefunction decays substantially, and the phase accumulated by charge carriers during their transit cannot be ignored, influencing their behavior [50]. The propagation of the charge carriers through the junction as well as through the superconductor/nonsuperconductor interface occurs through a special phenomenon called Andreev reflection. If in the absence of a barrier between the superconductor and non-superconductor the energy of the electron is higher than the superconducting gap, $E >> \Delta$ they simply pass through the interface. However, when $E < \Delta$ the electron can't enter superconductor as there are no energy states in the gap. Instead, the electron is reflected back as a hole, effectively transferring a charge of 2e into the superconductor, where the electron pairs decay into the condensate state [4, 52].

4.1.3 Quantum Hall effect

When subjected to a strong perpendicular magnetic field, graphene enters the quantum Hall effect (QHE) regime. In this state, the Hall resistance (Rxy) becomes quantized, while the longitudinal resistance (Rxx) drops to zero, except for peaks at specific magnetic field values. This phenomenon arises from the formation of quantized energy levels in the system, known as Landau levels (LLs). For a classical two-dimensional electron gas, the system's behavior can be described by the following Hamiltonian:

$$H = \frac{1}{2m}(\mathbf{p} + e\mathbf{A})^2 \quad \mathbf{A} = By\hat{x} \tag{34}$$

for which we can consider the wavefunction $\Psi(x, y) = \exp(ik_y y)\,\Phi(y)$. With that, we obtain

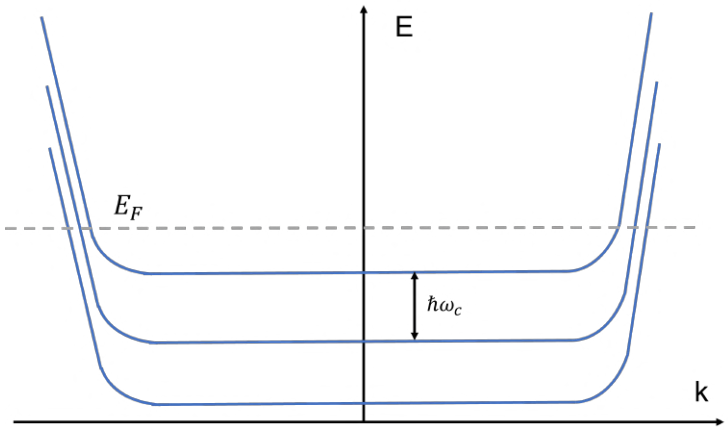

Figure 26: Bending of the Landau levels at the edges of a sample in the quantum Hall regime.

$$\frac{1}{2m}\left(-\hbar^2\frac{d^2}{dy^2}+(eB)^2\left(y-\frac{\hbar k_x}{eB}\right)^2\right)\Phi=E\Phi. \tag{35}$$

This equation is equivalent to a harmonic oscillator with frequency $\omega_c = eB/c$ (called cyclotron frequency) and energy levels where N corresponds to a number of formed Landau levels. The resulting energy spectrum for electrons is then

$$E_N=\hbar w_c\left(N+\frac{1}{2}\right)+V(y). \tag{36}$$

Each electron in the system undergoes cyclotron motion, which localizes them and prevents electrical conduction within the bulk of the material. However, near the edges of the system, electrons encounter a confining potential that increases their energy. As a result, the Landau levels bend near the edges of the system (Fig. 26). As a result, for each electron at the edge, the number of available states is equal to the number of filled Landau levels in the system. The slope of the confining potential outcomes in the appearance of the local electric field $\mathcal{E}_y = -\partial_y V(y)$. Since the electric field is consistently directed toward the bulk of the sample, the velocities of the electrons at opposite edges of the sample are oriented in opposite directions.

The previous example analyzed a classical electron gas characterized by parabolic energy dispersion, which leads to evenly spaced energy levels. In contrast, graphene features linear energy dispersion, which significantly influences the formation of Landau levels. For the two-dimensional Dirac electron gas (2DEG), we can adopt a similar methodology, starting instead with the Hamiltonian that describes Dirac electrons (eq(11)).

$$H=v\vec{\sigma}\cdot(\vec{p}+e\vec{A})=-i\hbar v\vec{\sigma}\cdot\left(\vec{\nabla}+i\frac{e}{\hbar}\vec{A}\right) \tag{37}$$

Considering the same wave function as in classical 2DEG we obtain the energy levels

$$E_N = \pm\hbar\omega_c\sqrt{N}. \tag{38}$$

The positive and negative signs correspond to the electron and hole sides, respectively, with the zero level being shared. Consequently, the resulting energy spectrum of Landau levels (LLs) is no longer equally spaced but varies as a function of $\sqrt{N}$. Next, we will calculate the LL degeneracy, which involves determining the number of cyclotron radii within a sample of dimensions L_x and L_y. The centers of two neighboring circular trajectories must be separated by $\Delta x = \frac{\hbar}{\Delta k_y eB}$. Given that $k_y = \frac{2\pi i}{L_y}$ due to periodic boundary conditions, we find that $\Delta x = \frac{\hbar}{eB} \cdot \frac{2\pi}{L_y} = \frac{h}{eBL_y}$. Therefore, the LL degeneracy is given by $N'_{LL} = \frac{L}{\Delta x} = \frac{L_x L_y eB}{h}$. The LL degeneracy per unit area is then $N_{LL} = \frac{eB}{h}$. For graphene, this value must also be multiplied by a degeneracy factor g, which equals 4. From this we can derive the filling factor, defined as the ratio between the carrier density and the number of LLs occupied.

$$\nu = \frac{n}{N_{LL}} = \frac{nh}{eB} \tag{39}$$

We notice that for graphene (and 2DEG in general) for a constant ν we reached a linear relation between magnetic field and carrier density. This results in the Hall conductance for graphene being

$$\sigma_{xy} = g\left(N + \frac{1}{2}\right)\frac{e^2}{h}. \tag{40}$$

We perform measurements of the graphene system under a magnetic field in a two-terminal system, shown in Fig. 27. In this setup up currents from the two contacts will enter different edge states and propagate to the opposite contact. As, for example, shown in Fig. 27 the current from the left contact enters the lower edge states and the current from the right contact propagates through the upper edge. The currents exceeding the contact are in equilibrium with the contact they come from. This means that if we measure the voltage drop anywhere on the same side of the sample, we get a longitudinal voltage drop $V_L = 0$, and if we measure the voltage probe between two points anywhere on different edges, we will obtain a Hall voltage drop $V_H = \mu_1 - \mu_2$(for simplicity we considered the case of high magnetic field, such that the edge states are not overlapped). Thus, in a two-terminal measurement, the observed signals represent a mixture of longitudinal and Hall contributions. However, at elevated magnetic fields, specifically within the Hall plateaus where the longitudinal signal vanishes, we expect to detect a clear Hall resistance [22, 53].

The measurements of the differential resistance as a function of magnetic field and gate voltage are shown in Fig. 28. We observe a clear emergence of Hall plateaus at filling

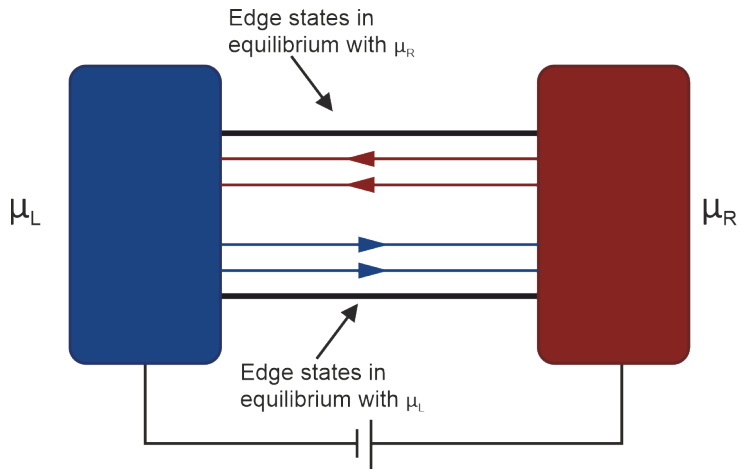

Figure 27: Two terminal measurement of a conductor in quantum Hall regime. The edge state carrying the current to the left is in equilibrium with the right contact. The edge state carrying the current to the right is in equilibrium with the left contact. The figure adapted from [20].

factors 2,6,10, and so on. The oscillations of the differential resistance, called Shubnikov-de Haas oscillations, start to be visible at a low magnetic field of $\sim$ 300 mT, and the first hall plateaus are formed by $\sim$ 1T (Fig. 29). The formation of Hall plateaus starts to occur at lower fields for the electron side, which indicates the effect of the npn cavity on the magnetotransport measurement of the device.

Fig. 28 illustrates the anticipated linear relationship between magnetic field B and charge carrier density n at a specific filling factor for the 2DEG system. This linear dependence allows us to derive the relationship between n and the gate voltage V_g. Utilizing equation eq(39), we find that at Hall plateaus, where the differential resistance is constant, the electron density is given by:

$$n(B) = \frac{B\nu h}{e} \tag{41}$$

Thus, the slope of the Hall plateau stripes is given by $\frac{dn}{dB} = \frac{\nu e}{h} = \frac{\nu}{\phi_0}$, with ϕ_0 denoting the magnetic flux quantum. In our experimental setup, the hBN/graphene system with the applied voltage to the gate acts as a parallel plate capacitor. This implies that by extracting the correlation between gate voltage and carrier density, we can calculate the capacitance of the system per unit area.

$$n = \frac{CV_g}{e} \tag{42}$$

The capacitance of the system is then

$$C = \frac{e\nu}{\Phi_0}\frac{dB}{dV}. \tag{43}$$

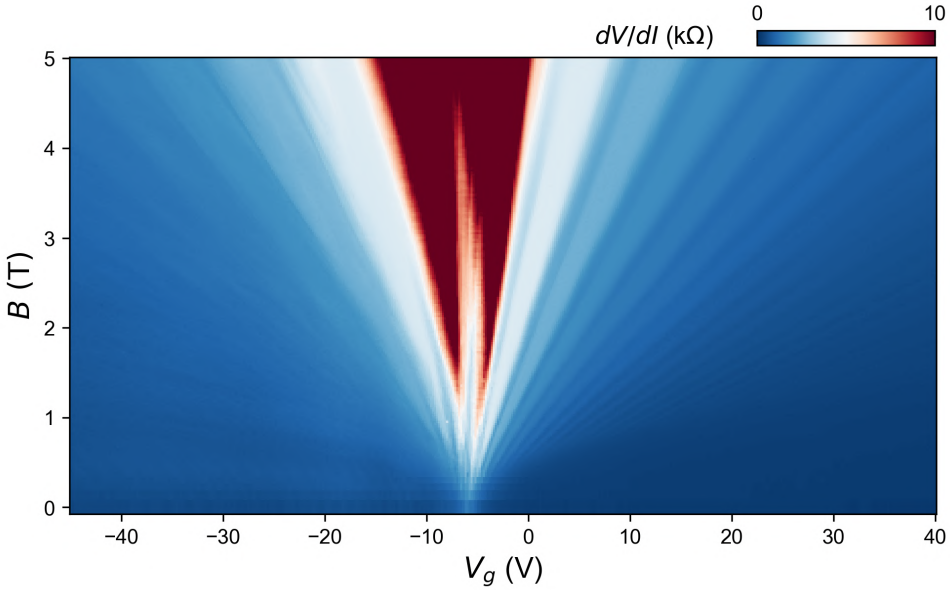

Figure 28: Landau fan measurements performed in graphene Josephson junction.

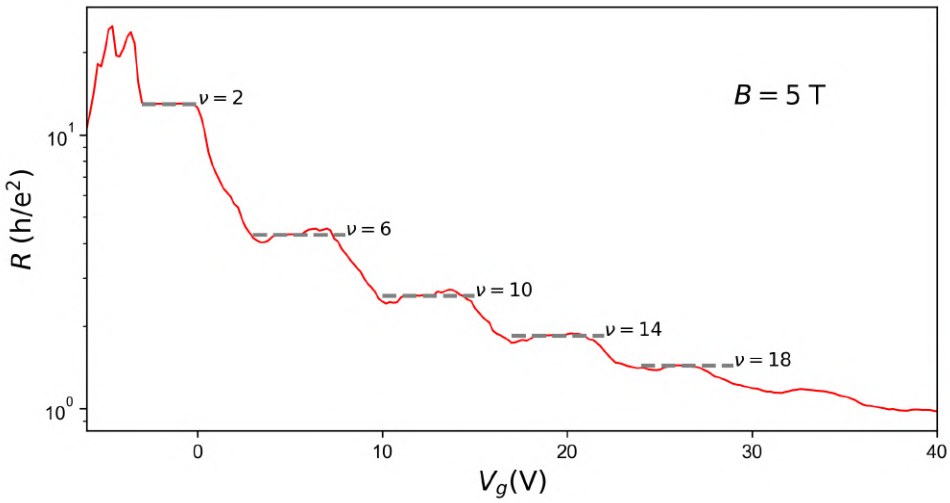

Figure 29: Measurement of the resistance of the junction with the change of the voltage gate at the magnetic field 5T. Gray dashed lines indicate the expected quantized resistance values.

The obtained capacitance for JJ1 is 9.76 nF/cm^2. This knowledge allowed us to plot the behavior of the graphene against carrier density and conduct analysis, which was done in the previous text.

4.2 Aligned graphene sample

We now turn our attention to graphene samples encapsulated in hBN, where the graphene flake is aligned with one of the hBN layers. We will begin with the same set of measurements discussed earlier, allowing us to identify the primary features introduced by the moiré potential. This will be followed by a detailed analysis of Fabry-Pérot oscillations and the supercurrent interference. Finally, we will discuss the high-field proximity observed in the JJs.

For this study, four junctions were fabricated and measured, each with a width of 1.5μm and lengths of 0.2μm, 0.3μm, 0.5μm, and 0.6μm. We begin by examining the resistance as a function of silicon gate voltage, as shown in Fig. 30. The key feature that indicates the formation of a moiré superlattice is the appearance of two satellite peaks symmetrically positioned with respect to the CNP. These peaks arise from the formation of satellite Dirac points (SDP). We notice that the DP on the electron (eDP) side is much less pronounced in comparison with the hole DP (hDP), whose resistance is comparable to that of the CNP.

We observe that the positions of the satellite peaks vary in carrier density across different junctions, which can be attributed to variations in the twist angles between the graphene and hBN layers in each sample. To estimate the twist angle for each junction, we first determine the capacitance, following the same approach used for non-aligned samples. Since the Dirac cone in aligned samples remains unchanged and significant alterations in the band structure only occur in remoteness to the Dirac point, the Landau fan near the charge neutrality point should exhibit the same behavior. After this, we identify the carrier densities at which the satellite peaks emerge.

The formed moiré superlattice is characterized by its wavelength with the corresponding area of moiré unit cell $A = \frac{\lambda^2\sqrt{3}}{2}$. The new Dirac points are expected to form at the full filling of the unit cells $n_s = \frac{4}{A}$. By expressing the λ_m as a function of the charge carrier density, we obtain a relation for the moiré superlattice wavelength.

$$\lambda_m = \sqrt{\frac{8}{\sqrt{3}n}}$$

The maximum value of lambda occurs at the perfect alignment of hBN and graphene and equals approximately 14nm. With the increase of misalignment angle, lambda reduces. The misalignment angle can be calculated from eq(24). For our samples, we obtain wavelengths varying from 13 nm to 13.6 nm, corresponding to rotation angles from 0.21° to 0.38°. Despite all the JJs being fabricated on the same graphene flake, we observe variations in the relative twist angles. This suggests that during the fabrication process, either the graphene or hBN (or both) experienced deformation. Moreover, the satellite

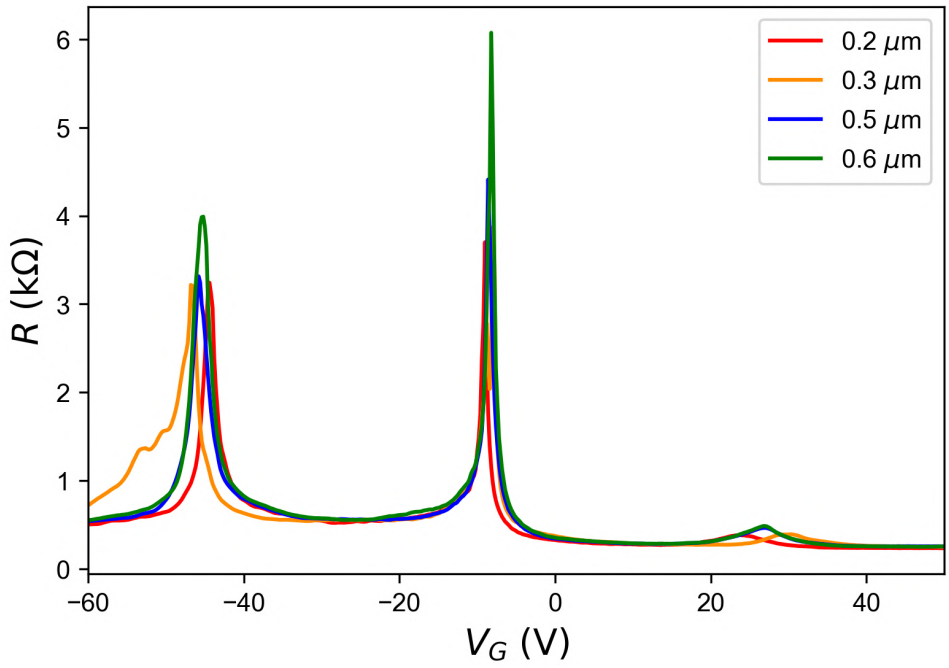

Figure 30: Resistance measurements of the junctions with graphene aligned to hBN.

peaks observed in JJ2 and JJ4 are not as sharp as those in the other junctions; instead, we see a primary peak with a smaller adjacent one.

As for the non-aligned samples, while conducting the measurements of R vs voltage gate at lower temperatures, we observe a drop of resistance to zero, which is explained by the proximity effect.

Differential resistance measurement shown in Fig. 31 shows clear proximity of the sample. While increasing the DC current going from negative to positive values we observe two peaks of differential resistance before drop of the resistance to zero. We also see that the superconducting region on this plot is asymmetric relative to the zero DC current, which is explained by so-called premature switching, which will be discussed later.

As for the non-aligned sample, we observe no proximity at CNP and superconducting pockets. The size of the pockets decays with the increasing length of the junction. We also, right as in the case with the non-aligned sample, see that the critical current for the electron side is generally larger than for the hole side. Similarly, as for the non-aligned sample, we address this issue to the formed npn cavities caused by n doping from the MoRe contacts. The situation is reversed in the case of the p-doping from the contacts as shown [48], where for the superlattice sample, a higher critical current was observed on the electron side. We also notice significant differences observed comparing eDP and hDP. For the hole side, in comparison with the electron side, we observe much higher normal resistance and absence of proximity. These effects can't be addressed to the electrode doping as in the case of p-doping, these features are preserved. This points out that the nature of this difference emerges from the difference in the band structure in the vicinity of the Dirac points.

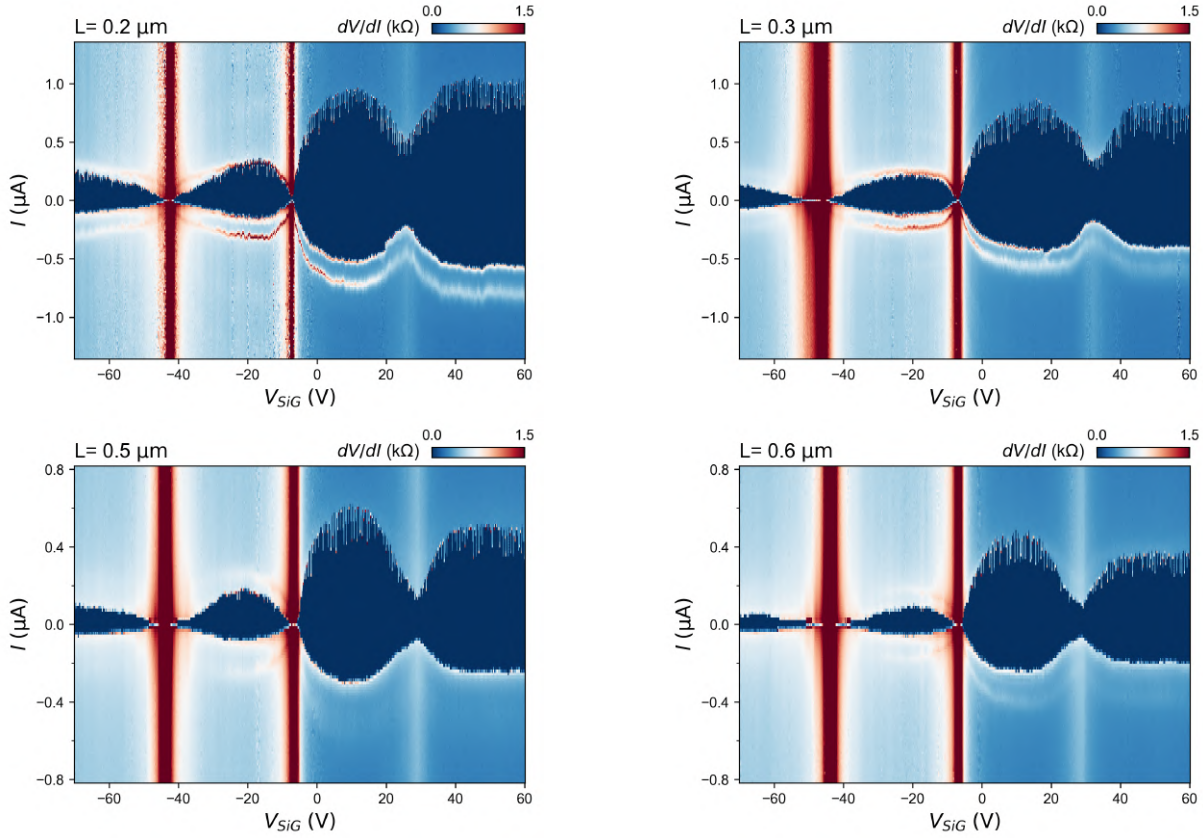

Figure 31: Differential resistance map measurements of four different junctions with graphene aligned to hBN. The measurements are performed at a temperature of 65 mK.

4.2.1 Ballistic regime. Fabry-Pérot oscillations

On the differential resistance maps, we observe asymmetric shapes of proximity pockets in the positive and negative current values. These two current values are called switching and retraping current, respectively. Switching and retraping currents are usually lower than the critical current of the system. The difference between these values is noticeable in our measurement with big random deviations of the switching current. Such behavior of the values can be addressed either by the underdamped regime of the junctions or by their overheating. In order to suppress the behavior and to be able to observe much clearer borders of proximity, we conduct the same measurement at a higher temperature, which is shown in Fig. 32. Now we can see that both critical and switching currents obtain more similar values, and the randomness of the switching current is significantly suppressed. This allows us to notice the oscillation of the critical current with frequency matching the oscillation of normal resistance at the same voltage gate values. The oscillations, similar to the case of non-aligned samples discussed above, are explained by Fabry-Pérot's interferometry of charge carriers propagating in a ballistic regime. The oscillations are visible to both sides of the hDP yet suppressed close to it.

For the FP with smooth potential, a following derivation for oscillation of current and conductance can be derived, as shown in [54]. Using the equation for resonance

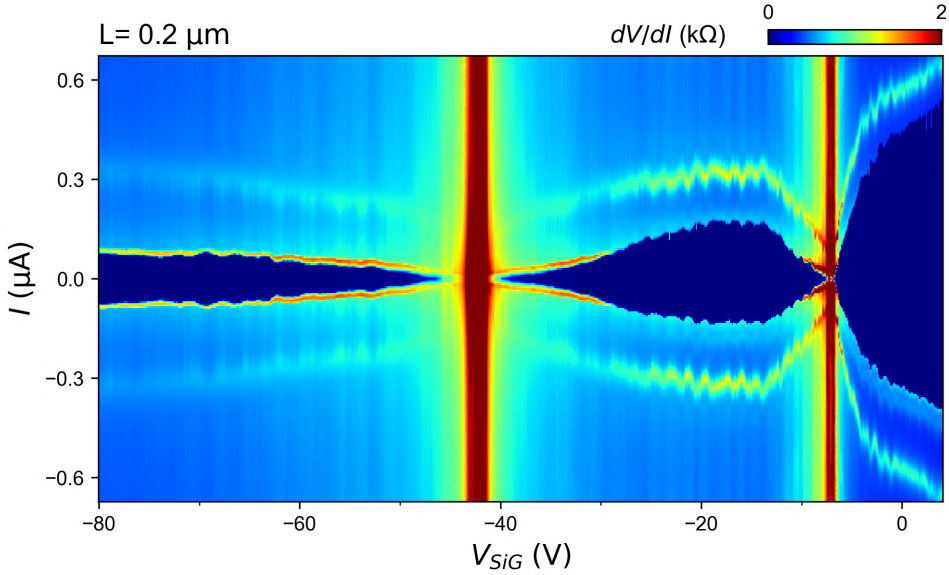

Figure 32: dV/dI map measurement performed at the temperature 2 K.

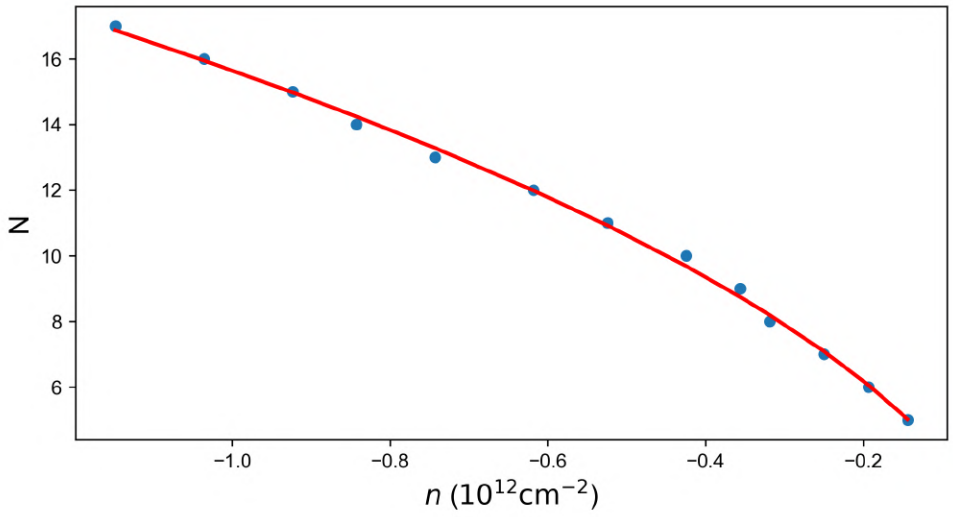

Figure 33: Fabry-Pérot oscillations for the aligned sample. Blue dots show the dependence of the number of the mode from the charge carrier density. The red line: the square root fit.

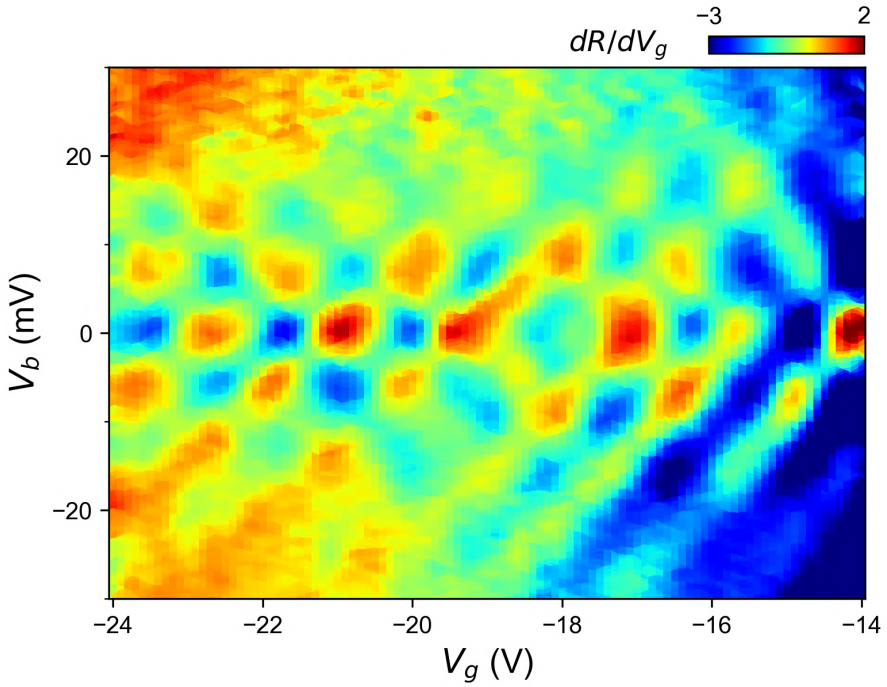

Figure 34: Change of the differential resistance with gate voltage as a function of gate voltage and bias voltage.

condition $2L_c/\lambda_F = N$ where L_c is the length of the cavity and dispersion relation eq(17) we can get the equation for dispersion relation $\varepsilon_0 = hv_F/2L_c$. Using the relation for the energy-dependent conductivity oscillations

$$G(\varepsilon) = G_0 + \delta G \sin(\frac{2\pi\varepsilon}{\varepsilon_0}), \tag{44}$$

we get an equation for the oscillation of the differential conductance

$$\frac{dI}{dV_b} = G_0 - \delta G \sin(\frac{2\pi\varepsilon_\mathrm{F}}{\varepsilon_0}) \cos(\frac{\pi e V_b}{\varepsilon_0}). \tag{45}$$

The expression shows that FP oscillations can be tuned not only by the change of a voltage gate but also by the change of the voltage bias. Measurement shown in Fig. 34 shows the changes in differential resistance as a function of both of the values. Qualitatively we observe the behavior expected by eq(45). We see FP oscillations as a function of both of these values forming a chequerboard-like dependence of differential resistance up to $V_b = 20\mathrm{mV}$. The deviation from predicted dependence can be explained by the change in the effective positions of the p-n junctions with the change of the gate voltage. As the periodicity of the chequerboard potential becomes smaller as we move away from CNP, one can conclude that the cavity length becomes bigger with increased hole doping of the graphene.

4.2.2 Supercurrent interference

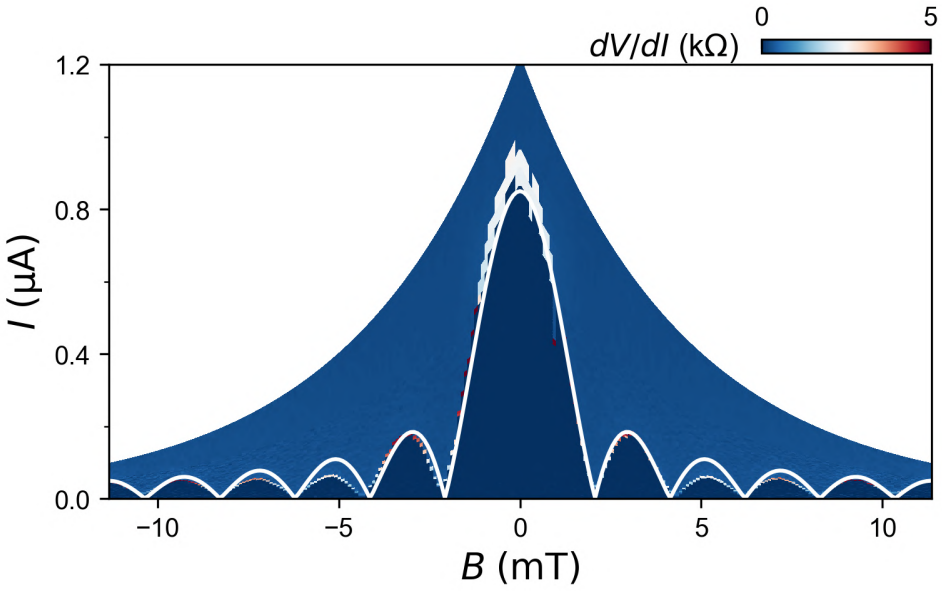

Figure 35: Oscillations of the supercurrent in JJ as a function of applied magnetic field. The white line indicates the Fraunhofer pattern.

Next, we observe the behavior of the junction in the presence of an external magnetic field. As expected, we observe the interference of a supercurrent. In relatively small magnetic fields, it follows the standard Fraunhofer pattern. At the fields > 5mT, we start to notice the deviation from the predicted behavior. As the periodicity of the oscillations preserves, the amplitude of the lobes is changed. When we extend the measurement to higher magnetic fields, the deviation from the Fraunhofer dependence becomes more obvious. The lobes of superconductivity preserve periodic behavior, however, at some magnetic fields we observe merging of neighbouring lobes. In the other values, we observe the absence of any noticeable superconductivity. Finally, we claim that at some point, the decaying of the maximum values of critical current stabilizes at some constant values. This feature is a signature of redistribution of the current flowing through the junction closer to its edges. The formation of edge currents under magnetic fields will play an important role in the discussion of the proximity effect at high magnetic fields in the following text.

4.2.3 Hofstadter butterfly

First, we focus on the general structure of the observed Landau fan measurement. As was mentioned in the theoretical introduction, the moiré structures are applicable for the observation of the Hofstadter butterfly. More generally, the effect can be observed only when the magnetic length $l_B = \sqrt{\hbar/eB}$ (the value characterizing the cyclotron motion of the charge carriers) is of the order of the wavelength of the periodic potential[39]. For example, for observation of the Hofstadter butterfly in the crystal lattice of non-aligned single-layer graphene, a magnetic field of $\sim$ 80kT is needed. Such a high value of the

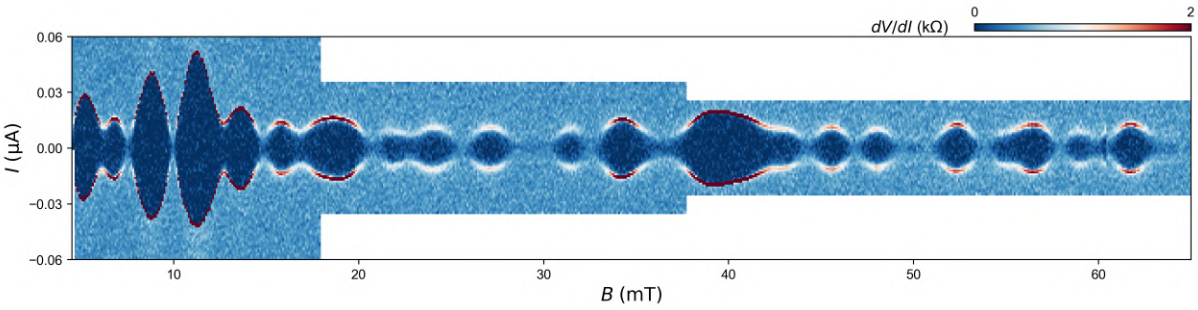

Figure 36: Oscillation of the critical current in the JJ at higher magnetic fields.

required field makes this effect impossible to observe. However, in the presence of moiré wavelength which values can reach $\sim$ 14nm for the hBN/graphene system, the required field is of achievable values $\sim$ 30T.

As shown by D. R. Hofstadter [37], the behavior of the system results in the self-similar recursive energy structure. Later, G. Wannier [55] came up with important insight into the system when adding carrier density into consideration. Replotting the Hofstadter butterfly into a density-field diagram (Wannier diagram), the Hofstadter butterfly transforms into a set of linear trajectories described by the Diophantine relation

$$\frac{n}{n_0} = t\frac{\phi}{\phi_0} + s, \tag{46}$$

where n and ϕ are carrier density and magnetic flux, n_0 and ϕ_0 are carrier density of a unit cell and magnetic flux quantum, t and s are integer values. In Fig. 37, the Landau fan measurement of the aligned sample is shown. We observe the emergence of the Hofstadter butterfly, which is demonstrated as a set of lines emerging from CNP and sDP, intercepting each other at fractional values of normalized magnetic flux.

4.2.4 High-field proximity

Fig. 38 shows the landau fan measurement done on the electron doping side. The dark blue regions indicate superconducting states, which are observed up to surprisingly high magnetic field values of $\sim$ 7T. We observe several distinct proximitized regions. We notice that in some of them the proximity is interrupted by random areas of normal state. Such different behaviors of superconductivity, as well as the shapes of the regions, are explained by the effect of the magnetic field on Andreev-bound states responsible for the proximity. The following is the discussion of these different regions:

1. The area marked with an orange line in Fig. 39 marks the region where the effect of the magnetic field on Andreev-bound states is insignificant. In the complete absence of a magnetic field electrons and holes have the opposite momenta and retrace trajectories of each other (Fig. 39b). The phases acquired in the junctions also cancel each other. The situation changes in the presence of the magnetic field

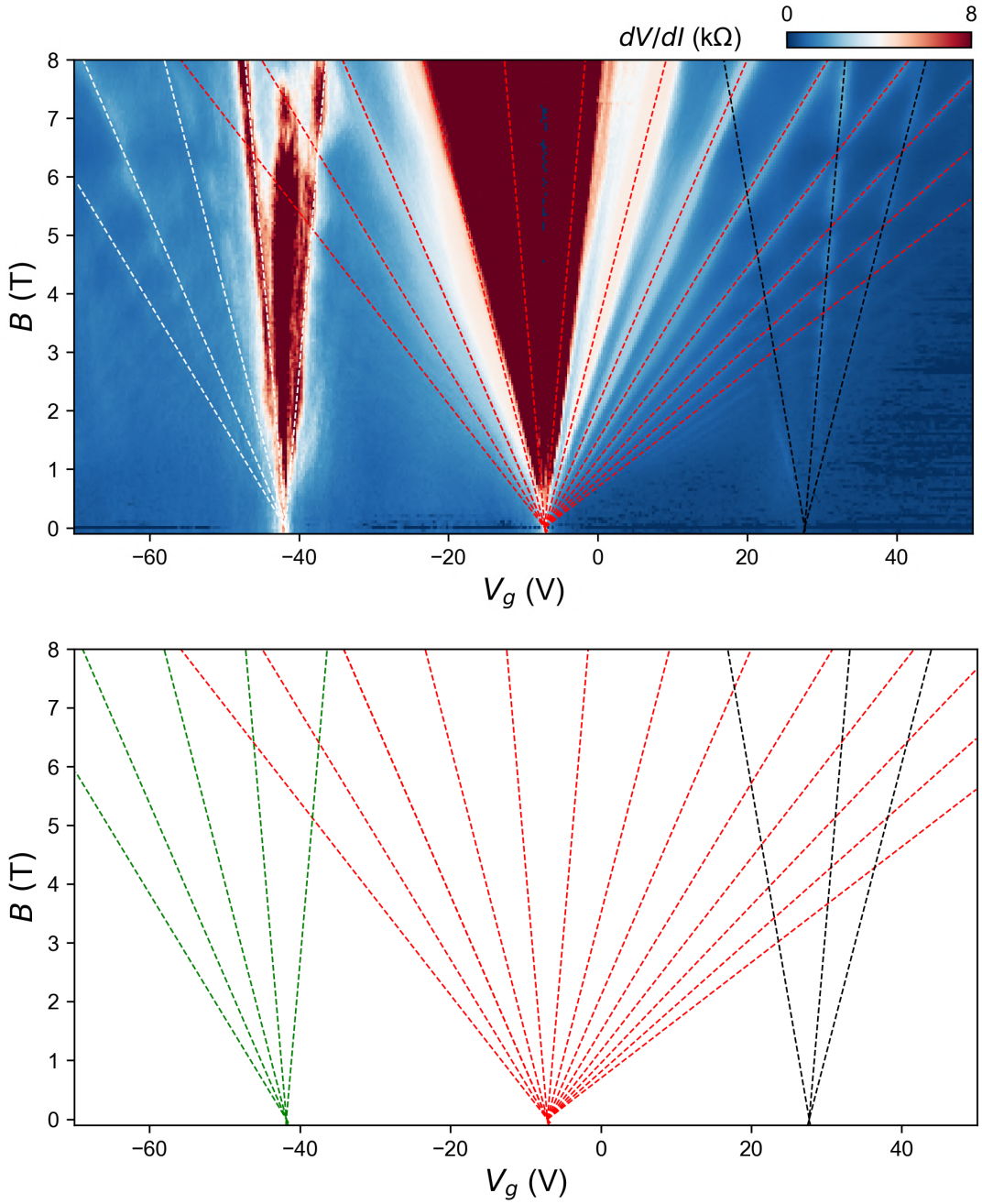

Figure 37: Emergence of Hofstadter butterfly in the aligned system. (a): Landau Fan diagram of the graphene sample aligned to hBN. Dashed lines indicate visible Hall states. (b): Schematics of Landau level visible in (a).

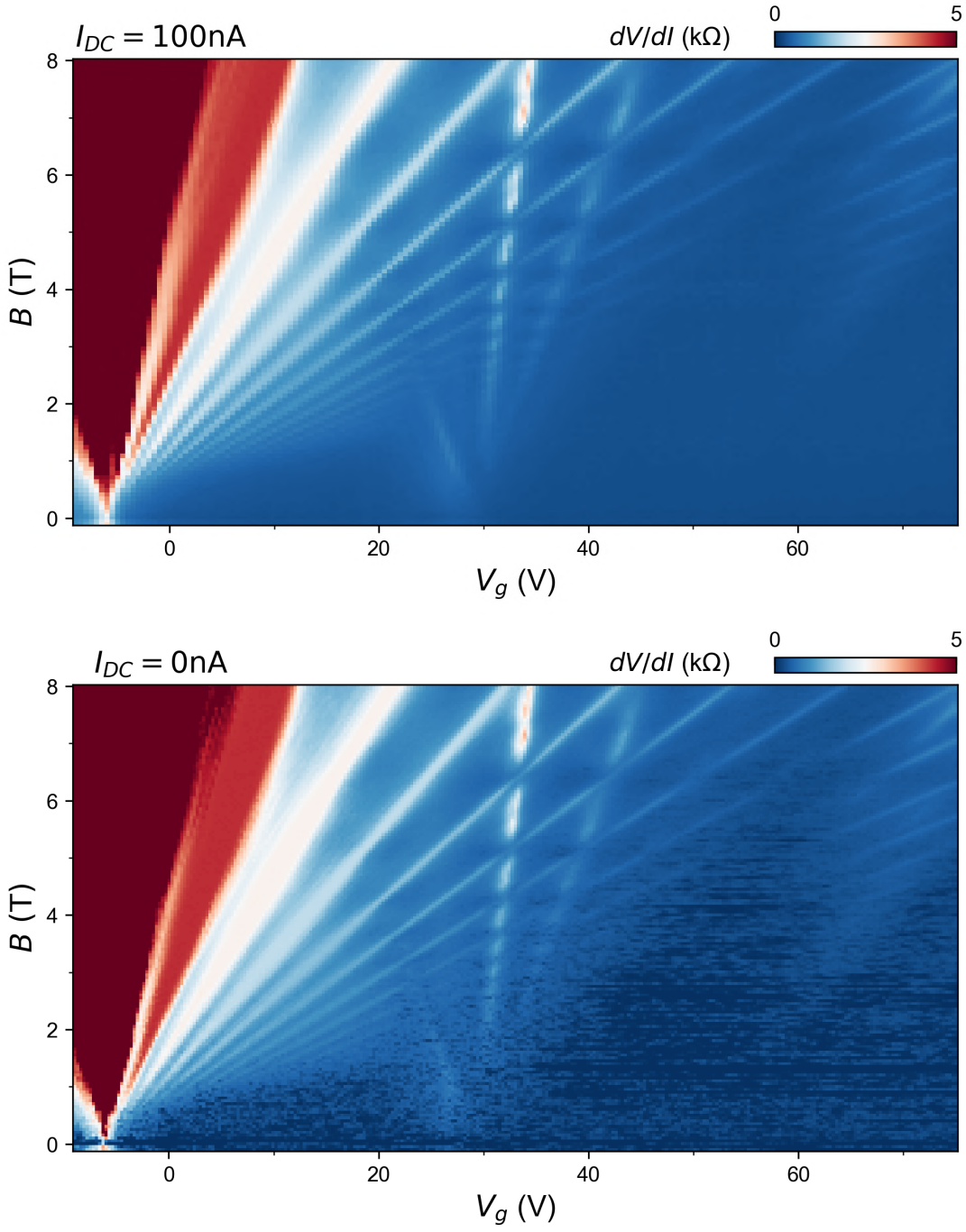

Figure 38: Landau Fan diagrams at electron doping of the graphene. (a): the measurement is performed at a bias current of 100 nA. (b): the measurement is performed at zero bias current.

when both electrons and holes acquire cyclotron trajectories. The proximity can still occur as long as the energy difference between holes and electrons is smaller than the superconducting gap, the phase difference is relatively small, and the trajectories are not separated by the values larger than coherence length and fermi wavelength (otherwise, the Cooper pair can not be formed)(Fig. 39c). In the [54], the maximum value of the magnetic field at which these conditions are agreed is estimated as $B^* \approx \Delta/eLv_f$, which approximately takes values of 5mT. Noticeably, around these values, we noticed the first deviation of supercurrent interference from the Fraunhofer pattern.

2. As the magnetic field is increased further, these conditions can no longer be fulfilled. As the cyclotron radius of the charge carriers is calculated as $r_c = \frac{p_F}{eB}$ the trajectories of the charge carriers deviate from each other further and further and create open trajectories (trajectories of the electrons and holes can not form a closed loop even after a number of reflections from the interfaces). In this case, the transfer of Cooper pairs is impossible. The situation is different, however, when one considers the trajectories affected by the edges of the sample. In this case, it is possible that the charge carriers form closed loops due to reflection from the edges (Fig. 39d). As the phase difference, in this case, is not zero but rather takes random values we observe fluctuation between superconducting and not superconducting state. In order to observe this regime, the cyclotron radius of the trajectories should be larger than half of the junction length $2r_c > L$. Using the dispersion relation for graphene, one can derive the equation for cyclotron radius as

$$r_c = \frac{P_F}{eB} = \frac{\hbar k_F}{eB} = \frac{\hbar\sqrt{\pi n}}{eB} \tag{47}$$

and then define the borders of the regime which is shown in the Fig. 39 with a yellow line.

3. At even higher magnetic fields, when $r_c < L/2$, the cyclotron radius becomes such small that the trajectories can fit in the junction without touching the opposite NS interface. The transfer of charge carriers can happen only by skipping edge orbits and the transfer of Cooper pairs can no longer happen by the mechanisms described above. Instead, we should observe the gradual formation of Landau levels. However, even at this regime, in the presence of formed Landau levels, we see random pockets of superconductivity (green region in the Fig. 39). As at such magnetic fields, the current must be mediated with the chiral edge states [56]. In order for proximity to occur the states should be coupled. As the width of the junction (1.5 μm) strongly exceeds the coherence length of the MoRe and cyclotron radius(at magnetic fields where landau splitting is observed) the coupling does not happen through direct transfer of charge carriers along N/S interface. Rather it happens through hybrid electron-hole modes formed at the N/S interface. The mechanism is sketched in the Fig. 39e. Once the electron in the edge state reaches the N/S interface, it turns into the hybrid e-h mode, which propagates along the interface until it reaches the opposite edge of the device. There, it couples to the new edge state as a hole and propagates back to the first interface, where it transforms back to the hybrid state

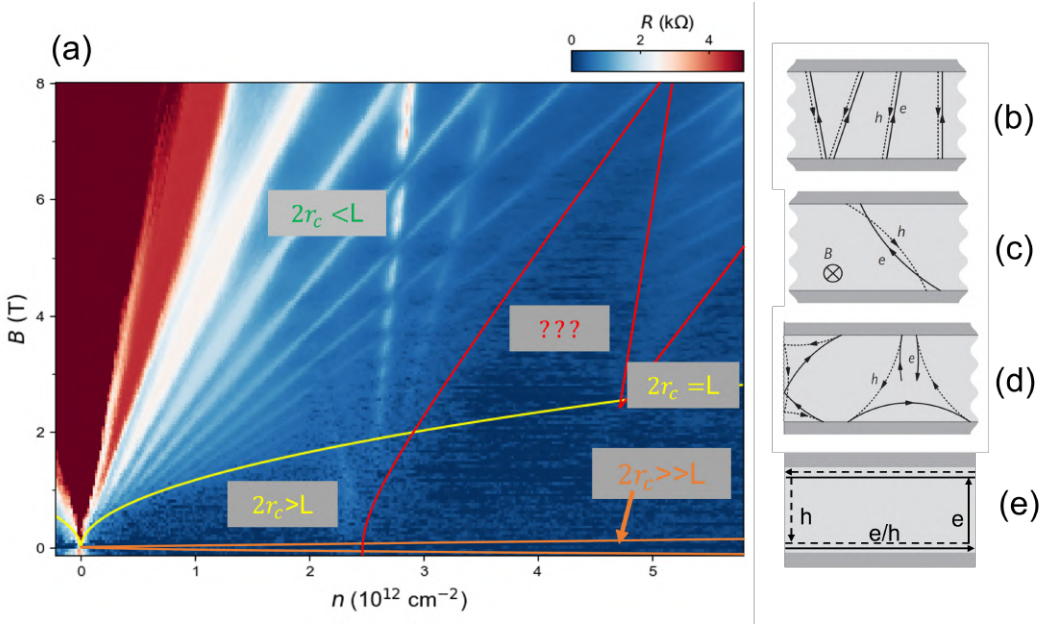

Figure 39: Proximity effect in the aligned hBN/graphene system. (a): Landau fan diagram with marked regions exhibiting different mechanisms of superconductivity discussed in the main text. (b) - (e): eletron-hole pairs under magnetic fields. (b): ballistic JJ with zero external magnetic field. (c): ballistic JJ under small magnetic field. (d): closed trajectories formed at the edge of the JJ under an intermediate magnetic field. (e): mechanism of proximity through the chiral edge states. Figures (b) - (d) are taken from [54]. Figure (e) is adapted from [56].

to propagate to the other edge and close the loop. This process allows the transfer of Cooper pairs through the edge states separated by significant distances [56].

4. Finally, we discuss the region of superconductivity where the proximity is observed at as high magnetic fields as 7T (marked with red color in the Fig. 39). We notice that the area emerges right at eDP. We also notice that in compare with the region of superconductivity carried by hybrid states, here we don't observe any presence of formed Landau levels. Indeed, if we complete the same Landau fan measurement but with a high current bias of 200μA to suppress any proximity, we notice that no Landau levels in the area are formed. We also state that eq(47) for the cyclotron frequency is not correct when reaching the eDP; as for its derivation, the approximation of linear dispersion relation was used, which is not appropriate once the Fermi energy is far from CNP. To find out whether the proximity mechanism here is similar and explained by the cyclotron radius being smaller than half of the length of the junction, one needs to find the relation between carrier density and the Fermi wave vector, which will reflect the band structure at eDP. The thesis concludes, leaving this question unresolved.

5 Conclusion

The following results were obtained from this thesis. First, we adjusted the recipe of the MoRe sputtering to achieve a robust superconducting contact to encapsulated graphene heterostructures. To do so, the effect of several physical processes preventing superconductivity and good contact between graphene and MoRe were considered. One of the main issues encountered was the deformation of the superconducting film due to thermal stress. Considering that, we adjusted the sputtering parameters to find good settings for a robust thin superconducting film deposition. To ensure the contact recipe reliably works, we measured the critical temperature of the resulting electrodes and the contact resistance using the transfer-length method. Both of the values are in agreement with the literature.

By implementing this recipe into the fabrication process, we were able to manufacture several devices of graphene-based Josephson junctions. Firstly, studied monolayer graphene samples non-aligned to the encapsulating hBN flakes. The estimated mobility of the carriers varies from $10^5 \mathrm{cm}^2\mathrm{V}^{-1}\mathrm{s}^{-1}$ to $2 \times 10^5 \mathrm{cm}^2\mathrm{V}^{-1}\mathrm{s}^{-1}$ for one of the devices. Such high mobility is the outcome of the good quality of the devices. The junctions also showed ballistic behavior, confirmed by observing Fabry-Pérot oscillations.

Secondly, we studied JJs, where the graphene was aligned to the hBN. The system exhibits the moiré pattern, which enables us to observe the Hofstadter butterfly. We concluded a ballistic regime of the junctions by detecting Fabry-Pérot oscillations, which we observed with the change of both voltage gate and voltage bias. Finally, we observed the superconducting proximity effect up to surprisingly high magnetic fields of 7 T. Although several mechanisms behind this phenomenon were discussed, the exact nature of superconducting proximity at such high fields remains unclear. The results obtained in this master thesis will hopefully inspire and motivate future research needed to understand this intriguing effect fully.

References

[1] K. S. Novoselov, A. K. Geim, S. V. Morozov, D. Jiang, Y. Zhang, S. V. Dubonos, I. V. Grigorieva, and A. A. Firsov. Electric Field Effect in Atomically Thin Carbon Films. *Science*, 306(5696):666–669, October 2004.

[2] H. Kamerlingh Onnes. Leiden comm. 120b, 122b, 124c. *Leiden Communications*, 120b, 122b, 124c, 1911.

[3] W. Meissner and R. Ochsenfeld. Ein neuer effekt bei eintritt der supraleitfähigkeit. *Naturwissenschaften*, 21:787, 1933.

[4] M. Tinkham. *Introduction to Superconductivity*. Dover Publications, 2nd edition, 2004.

[5] J. Bardeen, L. N. Cooper, and J. R. Schrieffer. Theory of superconductivity. *Phys. Rev.*, 108:1175–1204, 1957.

[6] V. L. Ginzburg and L. D. Landau. On the theory of superconductivity. *Zh. Eksp. Teor. Fiz.*, 20:1064, 1950.

[7] A. A. Abrikosov. On the magnetic properties of superconductors of the second group. *Zh. Eksp. Teor. Fiz.*, 32:1442–1452, 1957. [Sov. Phys. JETP 5, 1174 (1957)].

[8] J. G. Bednorz and K. A. M ller. Possible highT c superconductivity in the BaL-aCuO system. *Zeitschrift f r Physik B Condensed Matter*, 64(2):189–193, June 1986.

[9] Qing-Yan Wang, Zhi Li, Wen-Hao Zhang, Zuo-Cheng Zhang, Jin-Song Zhang, Wei Li, Hao Ding, Yun-Bo Ou, Peng Deng, Kai Chang, Jing Wen, Can-Li Song, Ke He, Jin-Feng Jia, Shuai-Hua Ji, Ya-Yu Wang, Li-Li Wang, Xi Chen, Xu-Cun Ma, and Qi-Kun Xue. Interface-Induced High-Temperature Superconductivity in Single Unit-Cell FeSe Films on SrTiO3. *Chinese Physics Letters*, 29:037402, March 2012. Publisher: IOP ADS Bibcode: 2012ChPhL..29c7402W.

[10] Defa Liu, Wenhao Zhang, Daixiang Mou, Junfeng He, Yun-Bo Ou, Qing-Yan Wang, Zhi Li, Lili Wang, Lin Zhao, Shaolong He, Yingying Peng, Xu Liu, Chaoyu Chen, Li Yu, Guodong Liu, Xiaoli Dong, Jun Zhang, Chuangtian Chen, Zuyan Xu, Jiangping Hu, Xi Chen, Xucun Ma, Qikun Xue, and X. J. Zhou. Electronic origin of high-temperature superconductivity in single-layer FeSe superconductor. *Nature Communications*, 3:931, July 2012. ADS Bibcode: 2012NatCo...3..931L.

[11] Shaolong He, Junfeng He, Wenhao Zhang, Lin Zhao, Defa Liu, Xu Liu, Daixiang Mou, Yun-Bo Ou, Qing-Yan Wang, Zhi Li, Lili Wang, Yingying Peng, Yan Liu, Chaoyu Chen, Li Yu, Guodong Liu, Xiaoli Dong, Jun Zhang, Chuangtian Chen, Zuyan Xu, Xi Chen, Xucun Ma, Qikun Xue, and X. J. Zhou. Phase diagram and electronic indication of high-temperature superconductivity at 65K in single-layer FeSe films. *Nature Materials*, 12:605–610, July 2013. ADS Bibcode: 2013NatMa..12..605H.

[12] Jian-Feng Ge, Zhi-Long Liu, Canhua Liu, Chun-Lei Gao, Dong Qian, Qi-Kun Xue,

Ying Liu, and Jin-Feng Jia. Superconductivity above 100 K in single-layer FeSe films on doped SrTiO3. *Nature Materials*, 14:285–289, March 2015. ADS Bibcode: 2015NatMa..14..285G.

[13] D. A. Wollman, D. J. Van Harlingen, W. C. Lee, D. M. Ginsberg, and A. J. Leggett. Experimental determination of the superconducting pairing state in YBCO from the phase coherence of YBCO-Pb dc SQUIDs. *Physical Review Letters*, 71(13):2134–2137, September 1993.

[14] Øystein Fischer, Martin Kugler, Ivan Maggio-Aprile, Christophe Berthod, and Christoph Renner. Scanning tunneling spectroscopy of high-temperature superconductors. *Reviews of Modern Physics*, 79(1):353–419, March 2007.

[15] T. Valla, A. V. Fedorov, Jinho Lee, J. C. Davis, and G. D. Gu. The Ground State of the Pseudogap in Cuprate Superconductors. *Science*, 314(5807):1914–1916, December 2006.

[16] Kiyohisa Tanaka, W. S. Lee, D. H. Lu, A. Fujimori, T. Fujii, Risdiana, I. Terasaki, D. J. Scalapino, T. P. Devereaux, Z. Hussain, and Z.-X. Shen. Distinct Fermi-Momentum-Dependent Energy Gaps in Deeply Underdoped Bi2212. *Science*, 314(5807):1910–1913, December 2006.

[17] Li Yu, D. Munzar, A. V. Boris, P. Yordanov, J. Chaloupka, Th. Wolf, C. T. Lin, B. Keimer, and C. Bernhard. Evidence for Two Separate Energy Gaps in Underdoped High-Temperature Cuprate Superconductors from Broadband Infrared Ellipsometry. *Physical Review Letters*, 100(17):177004, May 2008.

[18] M. C. Boyer, W. D. Wise, Kamalesh Chatterjee, Ming Yi, Takeshi Kondo, T. Takeuchi, H. Ikuta, and E. W. Hudson. Imaging the two gaps of the high-temperature superconductor Bi2Sr2CuO6+x. *Nature Physics*, 3(11):802–806, November 2007.

[19] B. D. Josephson. Possible new effects in superconductive tunnelling. *Phys. Lett.*, 1:251–253, 1962.

[20] Hideo Aoki. *Physics of Graphene*. NanoScience and Technology Ser. Springer International Publishing AG, Cham, 1st ed edition, 2014.

[21] P. R. Wallace. The Band Theory of Graphite. *Physical Review*, 71(9):622–634, May 1947.

[22] Hubert B. Heersche, Pablo Jarillo-Herrero, Jeroen B. Oostinga, Lieven M. K. Vandersypen, and Alberto F. Morpurgo. Bipolar supercurrent in graphene. *Nature*, 446(7131):56–59, March 2007.

[23] A. H. Castro Neto, F. Guinea, N. M. R. Peres, K. S. Novoselov, and A. K. Geim. The electronic properties of graphene. *Reviews of Modern Physics*, 81(1):109–162, January 2009.

[24] C. R. Dean, A. F. Young, I. Meric, C. Lee, L. Wang, S. Sorgenfrei, K. Watanabe, T. Taniguchi, P. Kim, K. L. Shepard, and J. Hone. Boron nitride substrates for

high-quality graphene electronics. *Nature Nanotechnology*, 5(10):722–726, October 2010.

[25] A. K. Geim and K. S. Novoselov. The rise of graphene. *Nature Materials*, 6(3):183–191, March 2007.

[26] Masa Ishigami, J. H. Chen, W. G. Cullen, M. S. Fuhrer, and E. D. Williams. Atomic Structure of Graphene on SiO $_2$. *Nano Letters*, 7(6):1643–1648, June 2007.

[27] M.I Katsnelson and A.K Geim. Electron scattering on microscopic corrugations in graphene. *Philosophical Transactions of the Royal Society A: Mathematical, Physical and Engineering Sciences*, 366(1863):195–204, January 2008.

[28] S. V. Morozov, K. S. Novoselov, M. I. Katsnelson, F. Schedin, D. C. Elias, J. A. Jaszczak, and A. K. Geim. Giant Intrinsic Carrier Mobilities in Graphene and Its Bilayer. *Physical Review Letters*, 100(1):016602, January 2008.

[29] Tsuneya Ando. Screening Effect and Impurity Scattering in Monolayer Graphene. *Journal of the Physical Society of Japan*, 75(7):074716, July 2006.

[30] Kentaro Nomura and A. H. MacDonald. Quantum Transport of Massless Dirac Fermions. *Physical Review Letters*, 98(7):076602, February 2007.

[31] E. H. Hwang, S. Adam, and S. Das Sarma. Carrier Transport in Two-Dimensional Graphene Layers. *Physical Review Letters*, 98(18):186806, May 2007.

[32] Jian-Hao Chen, Chaun Jang, Shudong Xiao, Masa Ishigami, and Michael S. Fuhrer. Intrinsic and extrinsic performance limits of graphene devices on SiO2. *Nature Nanotechnology*, 3(4):206–209, April 2008.

[33] J. Martin, N. Akerman, G. Ulbricht, T. Lohmann, J. H. Smet, K. Von Klitzing, and A. Yacoby. Observation of electron–hole puddles in graphene using a scanning single-electron transistor. *Nature Physics*, 4(2):144–148, February 2008.

[34] J. M. B. Lopes dos Santos, N. M. R. Peres, and A. H. Castro Neto. Graphene Bilayer with a Twist: Electronic Structure. *Physical Review Letters*, 99(25):256802, December 2007.

[35] Jiamin Xue, Javier Sanchez-Yamagishi, Danny Bulmash, Philippe Jacquod, Aparna Deshpande, K. Watanabe, T. Taniguchi, Pablo Jarillo-Herrero, and Brian J. LeRoy. Scanning tunnelling microscopy and spectroscopy of ultra-flat graphene on hexagonal boron nitride. *Nature Materials*, 10(4):282–285, April 2011.

[36] Régis Decker, Yang Wang, Victor W. Brar, William Regan, Hsin-Zon Tsai, Qiong Wu, William Gannett, Alex Zettl, and Michael F. Crommie. Local Electronic Properties of Graphene on a BN Substrate via Scanning Tunneling Microscopy. *Nano Letters*, 11(6):2291–2295, June 2011.

[37] Douglas R. Hofstadter. Energy levels and wave functions of Bloch electrons in rational and irrational magnetic fields. *Physical Review B*, 14(6):2239–2249, September 1976.

[38] Matthew Yankowitz, Jiamin Xue, Daniel Cormode, Javier D. Sanchez-Yamagishi, K. Watanabe, T. Taniguchi, Pablo Jarillo-Herrero, Philippe Jacquod, and Brian J. LeRoy. Emergence of superlattice Dirac points in graphene on hexagonal boron nitride. *Nature Physics*, 8(5):382–386, May 2012.

[39] C. R. Dean, L. Wang, P. Maher, C. Forsythe, F. Ghahari, Y. Gao, J. Katoch, M. Ishigami, P. Moon, M. Koshino, T. Taniguchi, K. Watanabe, K. L. Shepard, J. Hone, and P. Kim. Hofstadter's butterfly and the fractal quantum Hall effect in moiré superlattices. *Nature*, 497(7451):598–602, May 2013.

[40] B. Hunt, J. D. Sanchez-Yamagishi, A. F. Young, M. Yankowitz, B. J. LeRoy, K. Watanabe, T. Taniguchi, P. Moon, M. Koshino, P. Jarillo-Herrero, and R. C. Ashoori. Massive Dirac Fermions and Hofstadter Butterfly in a van der Waals Heterostructure. *Science*, 340(6139):1427–1430, June 2013.

[41] P. J. Zomer, M. H. D. Guimarães, J. C. Brant, N. Tombros, and B. J. Van Wees. Fast pick up technique for high quality heterostructures of bilayer graphene and hexagonal boron nitride. *Applied Physics Letters*, 105(1):013101, July 2014.

[42] D. G. Purdie, N. M. Pugno, T. Taniguchi, K. Watanabe, A. C. Ferrari, and A. Lombardo. Cleaning interfaces in layered materials heterostructures. *Nature Communications*, 9(1):5387, December 2018.

[43] P. Blake, K. S. Novoselov, A. H. Castro Neto, D. Jiang, R. Yang, T. J. Booth, A. K. Geim, and E. W. Hill. Making graphene visible. 2007. Publisher: arXiv Version Number: 3.

[44] Yuan Huang, Eli Sutter, Norman N. Shi, Jiabao Zheng, Tianzhong Yang, Dirk Englund, Hong-Jun Gao, and Peter Sutter. Reliable Exfoliation of Large-Area High-Quality Flakes of Graphene and Other Two-Dimensional Materials. *ACS Nano*, 9(11):10612–10620, November 2015.

[45] Jaemyung Kim, Franklin Kim, and Jiaxing Huang. Seeing graphene-based sheets. *Materials Today*, 13(3):28–38, March 2010.

[46] Jin Yong An and Yung Ho Kahng. Optical observation of single layer graphene on silicon nitride substrate. *AIP Advances*, 8(1):015107, January 2018.

[47] StenTech. Unveiling stentech bluprint™: Elite smt stencil treatment, February 2024. Accessed: 2024-10-22.

[48] V. E. Calado, S. Goswami, G. Nanda, M. Diez, A. R. Akhmerov, K. Watanabe, T. Taniguchi, T. M. Klapwijk, and L. M. K. Vandersypen. Ballistic Josephson junctions in edge-contacted graphene. *Nature Nanotechnology*, 10(9):761–764, September 2015.

[49] I.V. Borzenets, F. Amet, C.T. Ke, A.W. Draelos, M.T. Wei, A. Seredinski, K. Watanabe, T. Taniguchi, Y. Bomze, M. Yamamoto, S. Tarucha, and G. Finkelstein. Ballistic Graphene Josephson Junctions from the Short to the Long Junction Regimes. *Physical Review Letters*, 117(23):237002, December 2016.

[50] D.I. Indolese, R. Delagrange, P. Makk, J.R. Wallbank, K. Wanatabe, T. Taniguchi, and C. Schönenberger. Signatures of van Hove Singularities Probed by the Supercurrent in a Graphene-hBN Superlattice. *Physical Review Letters*, 121(13):137701, September 2018.

[51] K.I. Bolotin, K.J. Sikes, Z. Jiang, M. Klima, G. Fudenberg, J. Hone, P. Kim, and H.L. Stormer. Ultrahigh electron mobility in suspended graphene. *Solid State Communications*, 146(9-10):351–355, June 2008.

[52] AF Andreev. The thermal conductivity of the intermediate state in superconductors. , 46(5):1823–1828, 1964.

[53] Supriyo Datta. *Electronic Transport in Mesoscopic Systems*. Cambridge University Press, 1 edition, September 1995.

[54] M. Ben Shalom, M. J. Zhu, V. I. Fal'ko, A. Mishchenko, A. V. Kretinin, K. S. Novoselov, C. R. Woods, K. Watanabe, T. Taniguchi, A. K. Geim, and J. R. Prance. Quantum oscillations of the critical current and high-field superconducting proximity in ballistic graphene. *Nature Physics*, 12(4):318–322, April 2016.

[55] G. H. Wannier. A Result Not Dependent on Rationality for Bloch Electrons in a Magnetic Field. *physica status solidi (b)*, 88(2):757–765, August 1978.

[56] F. Amet, C. T. Ke, I. V. Borzenets, J. Wang, K. Watanabe, T. Taniguchi, R. S. Deacon, M. Yamamoto, Y. Bomze, S. Tarucha, and G. Finkelstein. Supercurrent in the quantum Hall regime. *Science*, 352(6288):966–969, May 2016.

Acknowledgement

First and foremost, I would like to express my sincere gratitude to my supervisor, Prof. Dmitri K. Efetov, for giving me the opportunity to join the group and providing guidance throughout this year. His drive to tackle challenging problems influenced the entire group, including myself. Being part of this team pushing the frontiers of physics is a great experience, both for personal and professional development. I have learned a lot under his guidance.

I also want to express my immense gratitude to Andrés Díez Carlón for being a fantastic supervisor throughout this past year. I am endlessly thankful for his daily effort to share his vast knowledge of physics and guide me through the world of research. His remarkable ability and desire to break down complex physics questions into simple concepts never ceased to amaze me. No matter how hard the challenges of the work were, I always felt his support.

I also want to thank my senior colleagues, Dr. Martin Lee and Dr. Rafael Luque Merino. Not a single day I was not amazed with their knowledge of physics. And not a single day I didn't appreciate their kindness and support. I thank Philipp Altpeter and Christian Obermayer for their help and shared wisdom during the cleanroom fabrication.

I extend my heartfelt thanks to my colleagues and friends - Jiazhuo, János, Hajar, and Leon. Joining the group on the same day, I found in them companions with whom I could share the experience of starting this new chapter of my life. They were there for me during tough days, and we celebrated the good ones together. Looking back on how many memories we have shared, it's hard to believe it has only been one year.

Finally, I extend my gratitude to all the members of the research group. Their positive and professional approach made this year truly enjoyable for me.

Declaration

I hereby declare that this thesis is my own work, and that I have not used any sources and aids other than those stated in the thesis.

München, 23.10.24

Author's signature